
Source-Free Adaptation to Measurement Shift via Bottom-Up Feature Restoration

Cian Eastwood^{*†} Ian Mason^{*†} Christopher K. I. Williams^{†‡} Bernhard Schölkopf[§]

[†] School of Informatics, University of Edinburgh

[‡] Alan Turing Institute, London

[§] Max Planck Institute for Intelligent Systems, Tübingen

Abstract

Source-free domain adaptation (SFDA) aims to adapt a model trained on labelled data in a source domain to unlabelled data in a target domain *without access to the source-domain data during adaptation*. Existing methods for SFDA leverage entropy-minimization techniques which: (i) apply only to classification; (ii) destroy model calibration; and (iii) rely on the source model achieving a good level of feature-space class-separation in the target domain. We address these issues for a particularly pervasive type of domain shift called *measurement shift*, characterized by a change in measurement system (e.g. a change in sensor or lighting). In the source domain, we store a lightweight and flexible approximation of the feature distribution under the source data. In the target domain, we adapt the feature-extractor such that the approximate feature distribution under the target data realigns with that saved on the source. We call this method *Feature Restoration* (FR) as it seeks to extract features with the same semantics from the target domain as were previously extracted from the source. We additionally propose *Bottom-Up Feature Restoration* (BUFR)—a bottom-up training scheme for FR which boosts performance by preserving learnt structure in the later layers of a network. Through experiments we demonstrate that BUFR often outperforms existing SFDA methods in terms of accuracy, calibration, and data efficiency, while being less reliant on the performance of the source model in the target domain.

1 Introduction

In the real world, the conditions under which a system is developed often differ from those in which it is deployed—a concept known as *dataset shift* (Quiñonero-Candela et al., 2009). In contrast, conventional machine learning methods work by ignoring such differences, assuming that the development and deployment domains match or that it makes no difference if they do not match (Storkey, 2009). As a result, machine learning systems often fail in spectacular ways upon deployment in the test or *target* domain (Torralba and Efros, 2011; Hendrycks and Dietterich, 2019; Recht et al., 2019; Geirhos et al., 2019).

One strategy might be to re-collect and annotate enough examples in the target domain to re-train or fine-tune the model (Yosinski et al., 2014; Luo et al., 2017). However, manual annotation can be extremely expensive. Another strategy is that of *unsupervised domain adaptation* (UDA), where unlabelled data in the target domain is incorporated into the development/training process. A common approach is to minimize the domain ‘gap’ by aligning statistics of the source and target distributions in feature space (Long et al., 2015, 2018; Ganin and Lempitsky, 2015; Ganin et al., 2016). However, these methods require simultaneous access to the source and target datasets—a requirement that is

^{*}Equal contribution.

Correspondence to c.eastwood@ed.ac.uk. Work completed while CE was an intern at MPI-IS Tübingen.

often impractical due to privacy regulations or transmission constraints. For example, deploying healthcare models (trained on private/sensitive data) to hospitals with different scanners, or deploying image-processing models (trained on huge amounts of data) to mobile devices with different cameras. Thus, *UDA without access to the source data at deployment time* has high practical value.

Recently, there has been increasing interest in methods to address this setting of *source-free domain adaptation* (SFDA, Kundu et al. 2020; Liang et al. 2020; Li et al. 2020; Morerio et al. 2020) where the source dataset is unavailable during adaptation in the deployment phase. However, to adapt to the target domain, these methods employ entropy-minimizing techniques² which: (i) apply only to classification (discrete labels); (ii) destroy model calibration—minimizing prediction-entropy causes every sample to be classified (correctly or incorrectly) with extreme confidence; and (iii) assume that, in the target domain, the feature space of the unadapted source model contains reasonably-separated data clusters, where samples within a cluster tend to share the same class label. As demonstrated in Section 5, even the most innocuous of shifts can destroy this *initial feature-space class-separation*, and with it, the performance of these techniques.

We address these issues for a specific type of domain shift called *measurement shift* (Storkey 2009 called this “domain shift”). Measurement shift is characterized by a change in measurement system, or method of description, and is particularly pervasive in real-world machine learning systems. For example, medical imaging systems often fail when deployed to hospitals with different scanners (Zech et al., 2018; AlBadawy et al., 2018; Beede et al., 2020), and self-driving cars often struggle under “shifted” deployment conditions, such as natural variations in lighting (Dai and Van Gool, 2018) or weather conditions (Volk et al., 2019). Under the assumption of measurement shift, we often expect that, in the target domain, the same features (i) exist and (ii) discriminate well between the classes—if only we could re-extract or *restore* them. Building on this observation, we propose Feature Restoration (FR)—a method which seeks to extract features with the same semantics from the target domain as were previously extracted from the source domain, under the assumption that this is sufficient to restore model performance. At development time, we train a source model and then save a lightweight and flexible approximation of the feature distribution under the source data. At deployment time, we adapt the source model’s feature-extractor such that the approximate feature distribution under the target data aligns with that saved on the source. We additionally propose Bottom-Up Feature Restoration (BUFR)—a bottom-up training scheme for FR which significantly improves the degree to which features are “restored” by preserving learnt structure in the later layers of a network. Through experiments we demonstrate that BUFR often outperforms existing SFDA methods in terms of accuracy, calibration, and data efficiency, while making less assumptions about the performance of the source model in the target domain (i.e. the initial feature-space class-separation).

2 Setting: source-free adaptation to measurement shift via FR

We now describe the two phases of source-free domain adaptation (SFDA), development and deployment, before explaining the assumption of measurement shift. For concreteness, we work with discrete outputs (i.e. classification) but FR can easily be applied to continuous outputs (i.e. regression).

Source-free adaptation. At **development time**, a source model is trained *with the expectation that an unknown domain-shift will occur upon deployment in the target domain*. Thus, the primary objective is to equip the model for source-free adaptation at deployment time. For previous work, this meant storing per-class means in feature space (Chidlovskii et al., 2016), generating artificial negative datasets (Kundu et al., 2020), or introducing special training techniques (e.g. label smoothing) that encourage tight, well-separated data clusters in feature space (Liang et al., 2020). For us, this means storing lightweight approximate parameterizations of the marginal feature distributions, as detailed in the next section. More formally, a source model $f_s : \mathcal{X}_s \rightarrow \mathcal{Y}_s$ is trained on n_s labelled examples from the source domain $\mathcal{D}_s = \{(\mathbf{x}_s^{(i)}, y_s^{(i)})\}_{i=1}^{n_s}$, with $\mathbf{x}_s^{(i)} \in \mathcal{X}_s$ and $y_s^{(i)} \in \mathcal{Y}_s$, before saving any lightweight statistics of the source data \mathcal{S}_s . At **deployment time**, we are given a pre-trained source model f_s , lightweight statistics of the source data \mathcal{S}_s , and n_t unlabelled examples from the target domain $\mathcal{D}_t = \{\mathbf{x}_t^{(i)}\}_{i=1}^{n_t}$, with $\mathbf{x}_t^{(i)} \in \mathcal{X}_t$. The goal is to learn a target model $f_t : \mathcal{X}_t \rightarrow \mathcal{Y}_t$ which accurately predicts the unseen target labels $\{y_t^{(i)}\}_{i=1}^{n_t}$, where $y_t^{(i)} \in \mathcal{Y}_t$. Importantly, the source dataset \mathcal{D}_s is not accessible during adaptation in the deployment phase.

²These can be direct (Grandvalet and Bengio, 2004) or indirect (via pseudo-labelling, Lee et al. 2013).

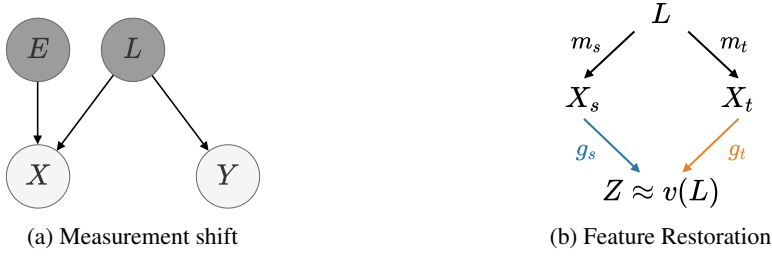


Figure 1: Measurement shift and the Feature Restoration principle.

Measurement shift. As depicted in Figure 1a, *measurement shift* (MS) can be understood by supposing some underlying, domain-invariant latent representation L of a sample (X, Y) . This combines with the domain (or environment) variable E to produce the observed covariates $X = m_E(L)$, where m_E is some domain-dependent mapping. For example, L could describe the shape, appearance and pose parameters of a number of objects comprising a scene, and the observations X are obtained by “rendering” the scene L , taking into account parameters in E that prescribe e.g. the lighting, camera properties, image corruption, background etc. Notice that the target variable Y depends *only* on L . Thus, to be a good predictor, our model *must* capture the information in L about Y . More specifically, let $Z = g_E(X)$ be our learned feature space, where our model f_E decomposes into a feature-extractor g_E , which depends on E , and a classifier h , with $f_E = h(g_E(X))$. Then the features Z *must* capture the information in L about Y with the variables in E acting as “nuisance variables” for obtaining this information from X . We desire an optimal $Z^* = v(L)$ for some (possibly non-invertible) function v , but in general we will have $Z = v(L) + \text{err}(E, L)$. In the source domain ($E = s$), training Z to predict Y will drive down the error (or noise) term $\text{err}(s, L)$. In the target domain ($E = t$), the nuisance variables in $E = t$ will initially drive up this error term once more, reducing the information about L in $Z = g_s(X)$ (and thus the information about Y in Z).

Feature Restoration. By learning a feature-extractor in the target domain g_t such that the distribution of Z is *restored*, i.e. $p(g_s(X_s)) \approx p(g_t(X_t))$, we drive down the error term in the target domain $\text{err}(t, L)$ and thus improve predictive accuracy. Figure 1b summarizes this idea. Here, the source X_s and target X_t data are “rendered” using domain-specific functions m_s and m_t respectively. In the source domain (left path), learning g_s to maximize predictive accuracy drives down the error term $\text{err}(s, L)$, leaving $Z \approx v(L)$. In the target domain (right path), learning g_t such that $p(Z)$ is *restored* drives down the error term $\text{err}(t, L)$, leaving $Z \approx v(L)$ once more. Ultimately, we desire that for any L we will have $g_s(m_s(L)) = g_t(m_t(L))$, i.e. that for source $X_s = m_s(L)$ and target $X_t = m_t(L)$ images generated from the same L , their corresponding Z ’s will match. Note that the MS assumption tells us that there *exists* a domain-invariant representation L , and L tells us everything we need to know about Y . Thus, *if* we can extract features Z in the source domain such that $Z \approx v(L)$, then we shouldn’t need to learn new features in the target domain in order to discriminate well between the classes—restoring our old features should be sufficient. However, it does not tell us whether or not it is possible to extract such a Z from the source domain. For example, predictors may exploit spurious correlations or “shortcuts” (Arjovsky et al., 2019; Geirhos et al., 2020) in the source domain (e.g. texture in photos) that are not available in the target domain (e.g. sketches). In Appendix A.4 we further discuss the assumptions required for FR, when they might be expected to hold, and analyse results on common UDA datasets where they do not hold (e.g. VisDA-C, Peng et al. 2018).

3 Feature Restoration

Below we detail the *Feature Restoration* (FR) framework. During development we train a model and then save a lightweight approximation of the feature distribution under the source data. At deployment time, we adapt the model’s feature-extractor such that the approximate feature distribution under the target data aligns with that saved on the source. Figure 2 gives an overview of the FR framework.

3.1 Development

Setup. The source model f_s is first trained using some loss, e.g. cross-entropy. Unlike most existing SFDA methods, we make no modification to the standard training process, allowing much time and money to be saved by utilizing pretrained source models. We decompose the source model f_s into a feature-extractor $g_s : \mathcal{X}_s \rightarrow \mathbb{R}^D$ and a classifier $h : \mathbb{R}^D \rightarrow \mathcal{Y}_s$, where D is the dimensionality of the feature space. So $\mathbf{z}_s^{(i)} = g_s(\mathbf{x}_s^{(i)})$ denotes the features extracted for source sample i , and

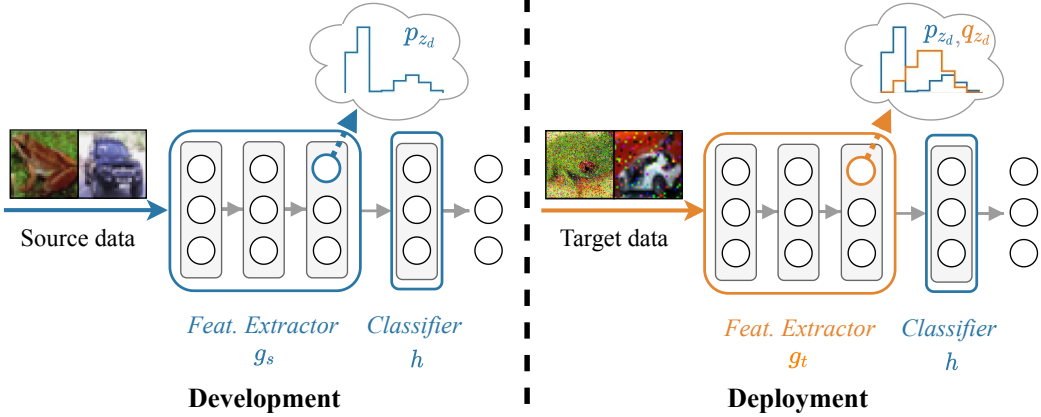


Figure 2: The Feature Restoration framework. *Left:* At development time, a source model is trained before saving approximations of the D marginal feature distributions under the source data $\{p_{z_d}\}_{i=1}^D$. *Right:* At deployment time, the feature-extractor is adapted such that the approximations of the marginal feature distributions on the target data $\{q_{z_d}\}_{i=1}^D$ align with those saved on the source.

$\hat{y}_s^{(i)} = f_s(\mathbf{x}_s^{(i)}) = h(g_s(\mathbf{x}_s^{(i)}))$ denotes the model’s output for source sample i . Under the assumption of measurement shift, the feature extractor should be adapted to unlabelled target data to give $\mathbf{z}_t^{(i)} = g_t(\mathbf{x}_t^{(i)})$, but the classifier h should remain unchanged, so that $\hat{y}_t^{(i)} = f_t(\mathbf{x}_t^{(i)}) = h(g_t(\mathbf{x}_t^{(i)}))$.

Choosing an approximation of the feature distribution. For high-dimensional feature spaces, storing the full joint distribution can be prohibitively expensive³. Thus, we choose to store only the marginal feature distributions. To accurately capture these marginal distributions, we opt to use soft binning (Dougherty et al., 1995) for its (i) *flexibility*—bins/histograms make few assumptions about distributional form, allowing us to accurately capture marginal feature distributions which we observe empirically to be heavily-skewed and bi-modal (see Appendix A.7); (ii) *scalability*—storage size does not scale with dataset size⁴, permitting very large source datasets (for a fixed number of bins B and features D , soft binning requires constant $O(BD)$ storage and simple matrix-multiplication to compute soft counts); and (iii) *differentiability*—the use of soft (rather than “hard”) binning, detailed in the next section, makes our approximation differentiable.

Estimating the parameters of our approximation on the source data. We now use the soft binning function of (Yang et al., 2018, Sec. 3.1) to approximately parameterize the D marginal feature distributions on the source data $\{p_{z_d}\}_{i=1}^D$, where p_{z_d} denotes the marginal distribution of the d -th feature z_d . Specifically, we approximately parameterize p_{z_d} using B normalised bin counts $\pi_{z_d}^s = [\pi_{z_d,1}^s, \dots, \pi_{z_d,B}^s]$, where $\pi_{z_d,b}^s$ represents the probability that a sample $z_d^{(i)}$ falls into bin b under the source data and $\sum_{b=1}^B \pi_{z_d,b}^s = 1$. $\pi_{z_d}^s$ is calculated using

$$\pi_{z_d}^s = \sum_{i=1}^{n_s} \frac{\mathbf{u}(z_d^{(i)})}{n_s} = \sum_{i=1}^{n_s} \frac{\mathbf{u}(g(\mathbf{x}^{(i)})_d; z_d^{min}, z_d^{max})}{n_s}, \quad (1)$$

where $z_d^{(i)} = g(\mathbf{x}^{(i)})_d$ denotes the d -th dimension of the i -th sample in feature space, \mathbf{u} is the vector-valued soft binning function (see Appendix A.1), $z_d^{min} = \min_{i=1}^{n_s} z_d^{(i)}$, and z_d^{max} is defined analogously to z_d^{min} . Repeating this for all D features, we get $\pi_z^s = [\pi_{z_1}^s, \pi_{z_2}^s, \dots, \pi_{z_D}^s]$. In the left-hand “cloud” of Figure 2, the blue curve depicts one such approximate marginal feature distribution $\pi_{z_d}^s$. We find it useful to additionally store approximate parameterizations of the marginal logit distributions on the source data $\pi_{\mathbf{a}}^s$, where the logit (i.e. pre-softmax) activations $\mathbf{a}^{(i)}$ are a linear combination of the feature activations $\mathbf{z}^{(i)}$, and $\pi_{\mathbf{a}}^s$ is defined analogously to π_z^s . Note that we can parameterize a similar distribution for regression. Intuitively, aligning the marginal logit distributions further constrains the ways in which the marginal feature distributions can be aligned. We validate

³If we assume the features are jointly Normal, the computational complexity is $O(ND^2)$ per update, where N is the mini-batch size on the target data. If instead we bin the joint feature space into histograms using B bins per dimension, the memory complexity is $O(B^D)$.

⁴Appendix A.1 (Table 5) specifies the storage size for various models and datasets.

this intuition empirically in the ablation study of Section 5.4. Finally, we equip the model for source-free adaptation at deployment time by saving the parameters/statistics of the source data $\mathcal{S}_s = \{\pi_{\mathbf{z}}^s, \pi_{\mathbf{a}}^s, \mathbf{z}^{min}, \mathbf{z}^{max}, \mathbf{a}^{min}, \mathbf{a}^{max}\}$, where $\mathbf{z}^{min} = [z_1^{min}, z_2^{min}, \dots, z_D^{min}]$ and $\mathbf{z}^{max}, \mathbf{a}^{min}$, and \mathbf{a}^{max} are defined analogously.

3.2 Deployment

At deployment time, we adapt the feature-extractor such that the approximate marginal distributions on the target data $(\pi_{\mathbf{z}}^t, \pi_{\mathbf{a}}^t)$ align with those saved on the source $(\pi_{\mathbf{z}}^s, \pi_{\mathbf{a}}^s)$. More specifically, we learn the target feature-extractor g_t by minimizing the following loss on the target data,

$$\mathcal{L}_{tgt}(\pi_{\mathbf{z}}^s, \pi_{\mathbf{z}}^t, \pi_{\mathbf{a}}^s, \pi_{\mathbf{a}}^t) = \sum_{d=1}^D D_{SKL}(\pi_{z_d}^s || \pi_{z_d}^t) + \sum_{k=1}^K D_{SKL}(\pi_{a_k}^s || \pi_{a_k}^t), \quad (2)$$

where $D_{SKL}(p || q) = \frac{1}{2}D_{KL}(p || q) + \frac{1}{2}D_{KL}(q || p)$ is the symmetric KL divergence, and $D_{KL}(\pi_{z_d}^s || \pi_{z_d}^t)$ is the KL divergence between the *distributions* parameterized by normalized bin counts $\pi_{z_d}^s$ and $\pi_{z_d}^t$, which is calculated using

$$D_{KL}(\pi_{z_d}^s || \pi_{z_d}^t) = \sum_{b=1}^B \pi_{z_d,b}^s \log \frac{\pi_{z_d,b}^s}{\pi_{z_d,b}^t}, \quad (3)$$

where $\pi_{z_d,b}^s$ represents the probability of a sample from feature d falling into bin b under the source data, and $\pi_{z_d,b}^t$ under the target data. Practically, to update on a batch of target samples, we first approximate $\pi_{\mathbf{z}}^t$ and $\pi_{\mathbf{a}}^t$ on that batch using Eq. 1, and then compute the loss. Appendix A.3 details the FR algorithm at development and deployment time, while Appendix A.11 summarizes the notations.

3.3 Bottom-Up Feature Restoration

A simple gradient-based adaption of g_t would adapt the weights of all layers at the same time. Intuitively, however, we expect that many measurement shifts like brightness or blurring can be resolved by only updating the weights of early layers. If the early layers can learn to extract the same features from the target data as they did from the source (e.g. the same edges from brighter or blurrier images of digits), then the subsequent layers shouldn’t need to update. Building on this intuition, we argue that adapting all layers simultaneously unnecessarily destroys learnt structure in the later layers of a network, and propose a bottom-up training strategy to alleviate the issue. Specifically, we adapt g_t in a bottom-up manner, training for several epochs on one “block” before “unfreezing” the next. Here, a block can represent a single layer or group of layers (e.g. a Residual block, He et al. 2016), and “unfreezing” simply means that we allow the block’s weights to be updated. We call this method *Bottom-Up Feature Restoration* (BUFR). In Section 5 we illustrate that BU training *significantly* improves accuracy, calibration, and data efficiency by preserving learnt structure in later layers of g_t .

4 Related work

Fine-tuning. A well-established paradigm in deep learning is to first pretrain a model on large-scale “source” data (e.g. ImageNet, Russakovsky et al. 2015) and then fine-tune the final layer(s) on the “target” data of interest (Girshick et al., 2014; Zeiler and Fergus, 2014). This implicitly assumes that new high-level concepts should be learned by recombining old (i.e. fixed) low-level features. In contrast, under the assumption of measurement shift, we fix the final layer and fine-tune the rest. This assumes that the same high-level concepts should be *restored* by learning new low-level features. Royer and Lampert (2020) fine-tune each layer of a network individually and then select the one that yields the best performance. For many domain shifts, they find it best to fine-tune an early or intermediate layer rather than the final one. This supports the idea that *which layer(s)* should update depends on *what* should be transferred.

Unsupervised DA. Inspired by the theory of Ben-David et al. (2007, 2010), many UDA methods seek to align source and target domains by matching their distributions in feature space (Long et al., 2015, 2018; Ganin and Lempitsky, 2015; Ganin et al., 2016; Sun and Saenko, 2016; Zellinger et al., 2017). In contrast to our work, these methods: (i) assume that the source and target domains share the same

feature-extractor; and (ii) require the source data during adaptation to align the feature distributions. While other methods have shown promise with domain-specific feature-extractors (Tzeng et al., 2017; Shu et al., 2018), they still require the source data during adaptation.

Source-free DA. Recently, Liang et al. (2020) achieved compelling results by re-purposing the semi-supervised information-maximization loss (Krause et al., 2010) and combining it with a pseudo-labelling loss (Lee et al., 2013). However, their entropy-minimizing losses are classification-specific, destroy model calibration, and rely on good initial performance of the source model in the target domain (feature-space class-separation, as demonstrated in the next section). Other works have trained expensive generative models so that the source data-distribution can be leveraged in the target domain (Li et al., 2020; Morerio et al., 2020; Kundu et al., 2020; Yeh et al., 2021). However, these methods are still classification-specific and rely on good initial feature-space class-separation for entropy minimization (Li et al., 2020; Kundu et al., 2020), pseudo-labelling (Morerio et al., 2020), and aligning the predictions of the source and target models (Yeh et al., 2021). Another approach is to focus specifically on the role of batch-normalization (BN) statistics. Li et al. (2017) propose Adaptive BN (AdaBN) where the BN-statistics of the source data are replaced with the BN-statistics of the target data. Remarkably, this simple parameter-free method is often competitive with more complex techniques. Schneider et al. (2020) and Nado et al. (2020) use very similar methods for adapting to covariate shift, while showing improvements in model calibration. Wang et al. (2021) also use the target data BN-statistics but additionally train the BN-parameters on the target data via entropy minimization, while focusing on an “online” setting. Our method also attempts to match statistics of the feature distributions, but is not limited to only matching the first two moments—hence can better handle non-Gaussian distributions.

Domain generalization. Domain generalization seeks to do well in the target domain *without updating the source model*. The goal is to achieve this through suitable data augmentation, self-supervision, and inductive biases with respect to a perturbation of interest (Simard et al., 1991; Engstrom et al., 2019; Michaelis et al., 2019; Roy et al., 2019; Djolonga et al., 2021). One may view this as specifying the shifts that a model should be robust to *a priori*. Practically, however, we generally do not know what shift will occur upon deployment—there will always be unseen shifts. Furthermore, the condition that our augmented development process be sufficiently diverse is untestable—with the worst-case error still being arbitrarily high (David et al., 2010; Arjovsky et al., 2019). Permitting adaptation in the target domain is one reasonable solution to these problems.

5 Experiments

In this section we evaluate our methods empirically on a number of datasets, each having multiple domains which can be seen in full in Appendix A.5. We compare our methods to various baselines, described below, before providing insight into *why* our method works through a detailed analysis.

5.1 Setup

Datasets. The simplest datasets we use are variations of the MNIST dataset (LeCun et al., 1998). Here, a model is trained on MNIST (source domain) before being adapted to MNIST-M (Ganin et al., 2016) or 1 of 15 MNIST-C (Mu and Gilmer, 2019) corruptions (target domain). Unfortunately, due to the small number of classes and relatively mild corruptions, the MNIST-based shifts can be well-resolved by a number of methods (accuracy $\geq 95\%$). Thus, to better facilitate model comparison, we additionally create and release EMNIST-DA—a domain adaptation (DA) dataset based on the 47-class Extended MNIST (EMNIST) character-recognition dataset (Cohen et al., 2017). EMNIST-DA contains 13 different shifts which were chosen to give a diverse range of initial accuracies when using a source model trained on the standard EMNIST dataset. In particular, a number of shifts result in very low initial performance but are conceptually simple to resolve (see Appendix A.5). Here, a model is trained on the training set of EMNIST (source domain) before being adapted to a shifted test set of EMNIST-DA (target domain, unseen examples). We also use the CIFAR-10-C and CIFAR-100-C corruption datasets (Hendrycks and Dietterich, 2019) to compare methods on more challenging object-recognition tasks. These datasets contain 19 different corruptions of the CIFAR-10 and CIFAR-100 *test sets*. Here, a model is trained on the training set of CIFAR-10/CIFAR-100 (source domain, Krizhevsky 2009) before being adapted to a corrupted test set (target domain).

Baselines. We show the performance of the source model on the source data as *no corruption*, and the performance of the source model on the target data (before adapting) as *source-only*. We also

Table 1: Digit and character accuracy (%) results. Shown are the mean and 1 standard deviation. *EMNIST-DA*: mean performance over all 13 EMNIST-DA shifts. *EMNIST-Svr* & *EMNIST-Mld*: sample “severe” and “mild” shifts from EMNIST-DA selected based on AdaBN performance⁵.

Model	MNIST-C	MNIST-M	EMNIST-DA	EMNIST-Svr	EMNIST-Mld
No corrupt.	99.5 ± 0.1	99.5 ± 0.1	89.4 ± 0.1	89.4 ± 0.1	89.4 ± 0.1
Source-only	86.2 ± 1.8	42.7 ± 4.6	29.5 ± 0.5	3.8 ± 0.4	78.5 ± 0.7
AdaBN	94.2 ± 0.2	59.1 ± 1.9	46.2 ± 1.1	3.7 ± 0.7	84.9 ± 0.2
PL	96.4 ± 0.4	43.1 ± 2.1	50.0 ± 0.6	2.7 ± 0.4	83.5 ± 0.1
IM	97.3 ± 0.2	66.9 ± 9.3	70.3 ± 3.7	24.0 ± 7.5	86.3 ± 0.1
SHOT	97.7 ± 0.2	94.4 ± 3.1	80.0 ± 4.4	55.1 ± 23.5	86.1 ± 0.1
FR (ours)	96.7 ± 0.1	86.5 ± 0.6	74.4 ± 0.8	15.3 ± 6.8	86.4 ± 0.1
BUFR (ours)	96.4 ± 0.6	96.2 ± 1.7	86.1 ± 0.1	84.6 ± 0.2	87.0 ± 0.2
Target-superv.	99.3 ± 0.0	98.5 ± 0.0	86.8 ± 0.6	85.7 ± 0.6	87.3 ± 0.7

implement the following baselines for comparison: *AdaBN* (Li et al., 2017) replaces the source BN-statistics with the target BN-statistics; *PL* is a basic pseudo-labelling approach (Lee et al., 2013); *IM* is the information-maximization loss from Liang et al. (2020) which consists of a prediction-entropy term and a prediction-diversity term; and *target-supervised* is an upper-bound that uses labelled target data (we use a 80-10-10 training-validation-test split, reporting accuracy on the test set). For digit and character datasets we additionally implement SHOT (Liang et al., 2020), which uses the IM loss along with special pre-training techniques (e.g. label smoothing) and a self-supervised PL loss. For object datasets we additionally implement TENT (Wang et al., 2021), which updates only the BN-parameters to minimize prediction-entropy, and also compare to some UDA methods—the self-supervised approach of Sun et al. (2019), denoted *UDA-SS*, and the adversarial approach of Ganin and Lempitsky (2015), denoted *UDA-Adv*. For all methods we report the classification accuracy and Expected Calibration Error (ECE, Naeini et al. 2015) which measures the difference in expectation between confidence and accuracy.

Implementation. For digit and character datasets we use a simple 5-layer convolutional neural network (CNN) which is a slight variation of LeNet (LeCun et al., 1998), and for object datasets we use ResNet-18 (He et al., 2016). For all datasets and methods we train using SGD with momentum set to 0.9, select the best-performing learning rate from $\{0.0001, 0.001, 0.01, 0.1, 1\}$, use a batch size of 256, and report results over 5 random seeds. For BUFR, we train for 30 epochs per block and decay the learning rate as a function of the number of unfrozen blocks in order to further maintain structure. For all other methods, including FR, we train for 150 epochs with a constant learning rate. The temperature parameter τ (see Appendix A.1, Eq. 4) is set to 0.01 in all experiments. Further implementation details are provided in Appendix A.9, while code to reproduce our results is available at <https://github.com/cianeastwood/bufr>.

5.2 Digit- and character-recognition results

Table 1 reports classification accuracies for the MNIST- and EMNIST-based datasets, while Appendix A.8 reports the corresponding ECEs (A.8.1) and full per-shift results (A.8.3 and A.8.4). On MNIST-C, where source-only accuracy is very high, all methods achieve good results—providing limited insight into their relative performances. On MNIST-M, our BUFR method beats all baselines, although SHOT is very similar in performance. Here, we largely attribute the sizable gap in performance between IM and SHOT to pre-training techniques (e.g. label smoothing). On EMNIST-DA, BUFR convincingly beats all other methods—particularly on severe shifts (penultimate column) where the initial feature-space class-separation is likely poor. Note the large deviation in performance across random runs for IM and SHOT, suggesting that initial feature-space clustering has a big impact on how well these entropy-minimization methods can separate the target data. This is particularly true for the severe shift, where only BUFR achieves high accuracy across random runs. For the mild shift, while all methods perform well, we still see that: (i) BUFR performs the best; and (ii) PL, IM and SHOT are quite poorly calibrated due to their entropy-minimizing (i.e. confidence-maximizing) objectives. In fact, these methods are only reasonably-calibrated if accuracy is very high. In contrast, our

⁵We find this to be a better indicator of shift severity than source-only, since some shifts with poor source-only performance can be well-resolved by simply updating the BN-statistics (no parameter updates), e.g. the fog shift.

Table 2: Object-recognition results. *Left*: Classification accuracy (%). *Right*: Expected Calibration Error (%). *: result adopted from Wang et al. (2021). Results show the mean and 1 standard deviation.

Model	CFR-10-C	CFR-100-C
No corrupt.	95.3 ± 0.2	76.4 ± 0.2
UDA-Adv.*	81.7	61.1
UDA-SS.*	83.3	53
Source-only	57.8 ± 0.7	36.4 ± 0.5
AdaBN	80.4 ± 0.1	56.6 ± 0.3
PL	82.5 ± 0.3	62.1 ± 0.2
IM	85.4 ± 0.2	67.0 ± 0.2
TENT	86.6 ± 0.3	66.0 ± 0.4
FR (ours)	87.2 ± 0.7	65.5 ± 0.2
BUFR (ours)	89.4 ± 0.2	68.5 ± 0.2
Target-superv.	88.4 ± 0.9	68.1 ± 1.2

Table 3: EMNIST-DA acc. vs. examples-per-class.

Model	5	10	20	50	400
PL	45.8	46.3	46.0	46.7	49.7
IM	48.3	51.7	51.2	54.7	73.4
FR	50.8	50.5	60.1	63.1	75.6
BUFR	78.0	82.3	83.8	84.9	86.2

Model	CFR-10-C	CFR-100-C
No corrupt.	2.4 ± 0.1	4.8 ± 0.1
UDA-Adv.	-	-
UDA-SS.	-	-
Source-only	28.2 ± 0.4	19.4 ± 0.9
AdaBN	11.2 ± 0.1	12.5 ± 0.1
PL	17.5 ± 0.3	37.7 ± 0.2
IM	14.6 ± 0.2	32.9 ± 0.2
TENT	12.8 ± 0.3	25.7 ± 0.4
FR (ours)	11.3 ± 0.3	15.7 ± 0.1
BUFR (ours)	10.0 ± 0.2	14.5 ± 0.3
Target-superv.	6.4 ± 0.6	9.6 ± 0.7

Table 4: Ablation study.

Model	CR-10-C	CR-100-C
\mathcal{L}_{tgt} w/o logits	86.7 ± 0.2	62.3 ± 1.3
\mathcal{L}_{tgt} w/o $D_{KL}(P Q)$	86.5 ± 0.3	61.5 ± 0.2
\mathcal{L}_{tgt}	87.2 ± 0.7	65.5 ± 0.2

methods maintain reasonable calibration as they do not work by making predictions more confident. This point is elucidated in the reliability diagrams and confidence histograms of Appendix A.6.

5.3 Object-recognition results

Table 2 reports classification accuracies and ECEs for CIFAR-10-C and CIFAR-100-C. Here we observe that our FR method is competitive with existing SFDA methods, while our BUFR method outperforms them on almost all fronts (except for ECE on CIFAR-100-C). We also observe the same 3 trends as on the digit and character datasets: (i) while the entropy-minimizing methods (PL, IM, TENT) do well in terms of accuracy, their confidence-maximizing objectives lead to higher calibration error—particularly on CIFAR-100-C where their ECE is even higher than that of the unadapted source-only model; (ii) the addition of bottom-up training significantly boosts performance; (iii) BUFR gets the largest boost on the most severe shifts—for example, as shown in the full per-shift results of Appendix A.8, BUFR achieves 89% accuracy on the impulse-noise shift of CIFAR-10-C, with the next best SFDA method achieving just 75%. Surprisingly, BUFR even outperforms target-supervised fine-tuning on both CIFAR-10-C and CIFAR-100-C in terms of accuracy. We attribute this to the regularization effect of bottom-up training, which we explore further in the next section.

We also evaluate our methods in the “online” setting of Wang et al. (2021), where we are restricted to a single pass through the corrupted test data, applying mini-batch updates along the way. As shown in Appendix A.8.2, our FR method outperforms existing SFDA methods on CIFAR-10-C and is competitive on CIFAR-100-C. This includes TENT (Wang et al., 2021)—a method designed specifically for this online setting.

5.4 Analysis

Feature-space class-separation. Measurement shifts can cause the target data to be poorly-separated in feature space. This point is illustrated in Figure 3 where we provide t-SNE visualizations of the feature-space class-separation on the EMNIST-DA crystals shift. Here, Figure 3a shows the initial class-separation *before* adapting the source model. We see that the source data is well separated in feature space (dark colours) but the target data is not (light colours). Figure 3b shows the performance of an entropy-minimization method when applied to such a “degraded” feature space where initial class-separation is poor on the target data. While accuracy and class-separation improve, the target-data clusters are not yet (i) fully homogeneous and (ii) returned to their original location (that of the source-data clusters). As shown in Figure 3(c,d), our methods of FR and BUFR better restore class-separation on the target data with more homogeneous clusters returned to their previous location.

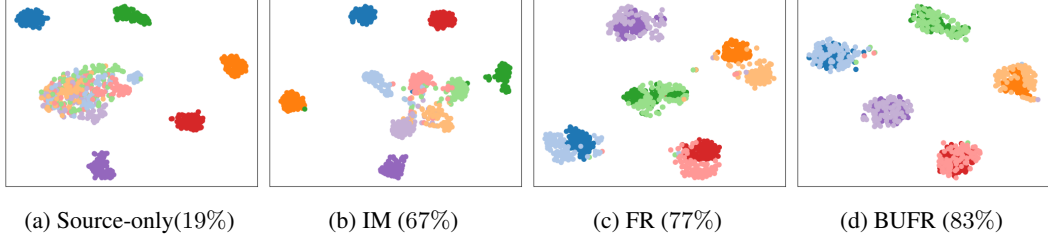


Figure 3: t-SNE (Van der Maaten and Hinton, 2008) visualization of features for 5 classes of the EMNIST-DA crystals shift. Dark colours show the source data, light colours the target. Model accuracies are shown in parentheses.

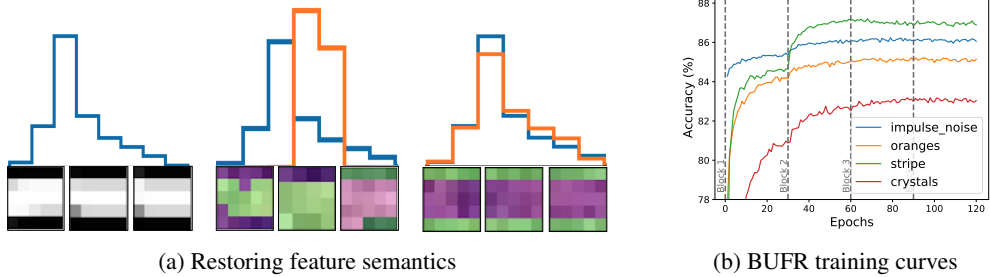


Figure 4: (a) Activation distributions (top) and maximally-activating image patches (bottom) for a specific filter in the first layer of a CNN. *Left*: Source model, source data (white digit, black background). *Centre*: Source model, target data (pink digit, green background). *Right*: Target model (adapted with BUFR), target data. (b) BUFR training curves on selected EMNIST-DA corruptions. Dashed-grey lines indicate when the next block is unfrozen.

Semantic meaning of features. The left column of Figure 4a shows the activation distribution (top) and maximally-activating image patches (bottom) for a specific filter in the first layer of a CNN trained on the standard EMNIST dataset (white digit, black background). The centre column shows that, when presented with shifted target data (pink digit, green background), the filter detects similar patterns of light and dark colours but no longer carries the same semantic meaning of detecting a horizontal edge. Finally, the right column shows that when our BUFR method aligns the marginal feature distributions on the target data (orange curve, top) with those saved on the source data (blue curve, top), this restores a sense of semantic meaning to the filters (image patches, bottom). Note that we explicitly align the *first-layer* feature distributions in this illustrative experiment.

Efficacy of BU training. Figure 4b shows that, when training in a bottom-up manner, updating only the first two blocks is sufficient to resolve many measurement shifts. This confirms the previous intuition that updating only the early layers should be sufficient for many measurement shifts. BUFR exploits this by primarily updating the early layers, thus preserving learnt structure in later layers (see Appendix A.10). To examine the regularization benefits of preserving learnt structure in later layers, we compare the accuracy of BUFR to other SFDA methods as the number of available target examples reduces. As shown in Table 3, the performances of IM and FR drop sharply as we reduce the number of available target examples. In contrast, BUFR maintains strong performance. With only 5 examples-per-class, it surpasses the performance of many baselines using all 400 examples-per-class.

Ablation study. We also conduct an ablation study on the components of our loss from Equation 2. Table 4 shows that, for easier tasks like CIFAR-10-C, aligning the logit distributions and using the symmetric KL divergence (over a more commonly-used asymmetric KL divergence) make little difference to performance. However, for harder tasks like CIFAR-100-C, both improve accuracy.

6 Discussions

Aligning the marginals may be insufficient. Our method seeks to restore the full joint feature distribution by aligning (approximations of) the marginals. While we found that this is often sufficient, it cannot be guaranteed unless the features are independent. One potential remedy is to encourage feature independence in the source domain using “disentanglement” methods (Higgins et al., 2017; Eastwood and Williams, 2018), allowing the marginals to better capture the joint.

Learning general features in the source domain can be difficult. As discussed in Section 2, the assumption of measurement shift assures us that “general” features exist (highly discriminative in the source *and* target domains), but not that it is possible to extract them from only the source domain. As discussed in Appendix A.4.1, the necessity of ImageNet pretraining for many common UDA tasks highlights the difficulty of doing so. One promising approach is to seek features that yield invariant predictive accuracy across multiple source domains (Peters et al., 2016; Arjovsky et al., 2019), where multiple source domains are available.

7 Conclusion

We proposed BUFR, a method for source-free adaptation to measurement shift. BUFR works by aligning the approximate marginal feature distributions on the target data with those saved on the source, using a bottom-up training scheme. We showed that, through the assumption of measurement shift, BUFR often outperforms existing methods in terms of accuracy, calibration and data efficiency, while making less assumptions about the behaviour of the source model on the target data. We also highlighted some issues with the entropy-minimizing techniques on which existing SFDA-methods rely, namely their classification-specificity, tendency to be poorly calibrated, and vulnerability to simple but severe shifts.

8 Acknowledgements

We thank Oisin Mac Aodha, Luigi Gresele, Julius von Kügelgen and the MPI Tübingen causality group for helpful discussions and comments.

CE acknowledges support from The National University of Ireland via his Travelling Studentship in the Sciences. IM is supported by the Engineering and Physical Sciences Research Council (EPSRC).

References

AlBadawy, E. A., Saha, A., and Mazurowski, M. A. (2018). Deep learning for segmentation of brain tumors: Impact of cross-institutional training and testing. *Medical Physics*, 45(3):1150–1158.

Arjovsky, M., Bottou, L., Gulrajani, I., and Lopez-Paz, D. (2019). Invariant risk minimization. *arXiv preprint arXiv:1907.02893*.

Beede, E., Baylor, E., Hersch, F., Iurchenko, A., Wilcox, L., Ruamviboonsuk, P., and Vardoulakis, L. M. (2020). A human-centered evaluation of a deep learning system deployed in clinics for the detection of diabetic retinopathy. In *Proceedings of the 2020 CHI Conference on Human Factors in Computing Systems*, page 1–12. Association for Computing Machinery.

Ben-David, S., Blitzer, J., Crammer, K., Kulesza, A., Pereira, F., and Vaughan, J. W. (2010). A theory of learning from different domains. *Machine Learning*, 79(1):151–175.

Ben-David, S., Blitzer, J., Crammer, K., and Pereira, F. (2007). Analysis of representations for domain adaptation. In *Advances in Neural Information Processing Systems*, pages 137–144.

Chidlovskii, B., Clinchant, S., and Csurka, G. (2016). Domain adaptation in the absence of source domain data. In *Proceedings of the 22nd ACM SIGKDD International Conference on Knowledge Discovery and Data Mining*, pages 451–460.

Cohen, G., Afshar, S., Tapson, J., and van Schaik, A. (2017). EMNIST: an extension of MNIST to handwritten letters. *arXiv preprint arXiv:1702.05373*.

Dai, D. and Van Gool, L. (2018). Dark model adaptation: Semantic image segmentation from daytime to nighttime. In *International Conference on Intelligent Transportation Systems*, pages 3819–3824. IEEE.

David, S. B., Lu, T., Luu, T., and Pál, D. (2010). Impossibility theorems for domain adaptation. In *Proceedings of the Thirteenth International Conference on Artificial Intelligence and Statistics*, pages 129–136.

DeGroot, M. H. and Fienberg, S. E. (1983). The comparison and evaluation of forecasters. *Journal of the Royal Statistical Society: Series D (The Statistician)*, 32(1-2):12–22.

Djolonga, J., Yung, J., Tschannen, M., Romijnders, R., Beyer, L., Kolesnikov, A., Puigcerver, J., Minderer, M., D’Amour, A., Moldovan, D., Gelly, S., Houlsby, N., Zhai, X., and Lucic, M. (2021). On robustness and transferability of convolutional neural networks.

Dougherty, J., Kohavi, R., and Sahami, M. (1995). Supervised and unsupervised discretization of continuous features. In *International Conference on Machine Learning*, pages 194–202.

Eastwood, C. and Williams, C. K. (2018). A framework for the quantitative evaluation of disentangled representations. In *International Conference on Learning Representations*.

Engstrom, L., Tran, B., Tsipras, D., Schmidt, L., and Madry, A. (2019). Exploring the landscape of spatial robustness. In *International Conference on Machine Learning*, pages 1802–1811.

Ganin, Y. and Lempitsky, V. (2015). Unsupervised domain adaptation by backpropagation. In *International Conference on Machine Learning*, pages 1180–1189. PMLR.

Ganin, Y., Ustinova, E., Ajakan, H., Germain, P., Larochelle, H., Laviolette, F., Marchand, M., and Lempitsky, V. (2016). Domain-adversarial training of neural networks. *Journal of Machine Learning Research*, 17(1):2096–2030.

Geirhos, R., Jacobsen, J.-H., Michaelis, C., Zemel, R., Brendel, W., Bethge, M., and Wichmann, F. A. (2020). Shortcut learning in deep neural networks. *Nature Machine Intelligence*, 2:665–673.

Geirhos, R., Medina Temme, C., Rauber, J., Schütt, H., Bethge, M., and Wichmann, F. (2019). Generalisation in humans and deep neural networks. In *Advances in Neural Information Processing Systems*, pages 7549–7561.

Girshick, R., Donahue, J., Darrell, T., and Malik, J. (2014). Rich feature hierarchies for accurate object detection and semantic segmentation. In *Proceedings of the IEEE Conference on Computer Vision and Pattern Recognition*, pages 580–587.

Grandvalet, Y. and Bengio, Y. (2004). Semi-supervised learning by entropy minimization. In *Advances in Neural Information Processing Systems*, pages 529–536.

Guo, C., Pleiss, G., Sun, Y., and Weinberger, K. Q. (2017). On calibration of modern neural networks. In *International Conference on Machine Learning*, pages 1321–1330.

He, K., Zhang, X., Ren, S., and Sun, J. (2016). Deep residual learning for image recognition. In *Proceedings of the IEEE Conference on Computer Vision and Pattern Recognition*, pages 770–778.

Hendrycks, D. and Dietterich, T. (2019). Benchmarking neural network robustness to common corruptions and perturbations. In *International Conference on Learning Representations*.

Higgins, I., Matthey, L., Pal, A., Burgess, C., Glorot, X., Botvinick, M., Mohamed, S., and Lerchner, A. (2017). β -VAE: Learning basic visual concepts with a constrained variational framework. In *International Conference on Learning Representations*.

Krause, A., Perona, P., and Gomes, R. (2010). Discriminative clustering by regularized information maximization. In *Advances in Neural Information Processing Systems*, pages 775–783.

Krizhevsky, A. (2009). Learning multiple layers of features from tiny images. Technical report.

Kundu, J. N., Venkat, N., Babu, R. V., et al. (2020). Universal source-free domain adaptation. In *Proceedings of the IEEE/CVF Conference on Computer Vision and Pattern Recognition*, pages 4544–4553.

LeCun, Y., Bottou, L., Bengio, Y., and Haffner, P. (1998). Gradient-based learning applied to document recognition. *Proceedings of the IEEE*, 86(11):2278–2324.

Lee, D.-H. et al. (2013). Pseudo-label: The simple and efficient semi-supervised learning method for deep neural networks. In *Workshop on Challenges in Representation Learning, ICML*, volume 3.

Li, R., Jiao, Q., Cao, W., Wong, H.-S., and Wu, S. (2020). Model adaptation: Unsupervised domain adaptation without source data. In *Proceedings of the IEEE/CVF Conference on Computer Vision and Pattern Recognition*, pages 9641–9650.

Li, Y., Wang, N., Shi, J., Liu, J., and Hou, X. (2017). Revisiting batch normalization for practical domain adaptation. In *International Conference on Learning Representations Workshop*.

Liang, J., Hu, D., and Feng, J. (2020). Do we really need to access the source data? source hypothesis transfer for unsupervised domain adaptation. In *International Conference on Machine Learning (ICML)*, pages 6028–6039.

Long, M., Cao, Y., Wang, J., and Jordan, M. (2015). Learning transferable features with deep adaptation networks. In *International Conference on Machine Learning*, pages 97–105.

Long, M., Cao, Z., Wang, J., and Jordan, M. I. (2018). Conditional adversarial domain adaptation. In *Advances in Neural Information Processing Systems*.

Luo, Z., Zou, Y., Hoffman, J., and Fei-Fei, L. (2017). Label efficient learning of transferable representations across domains and tasks. In *Advances in Neural Information Processing Systems*, page 164–176.

Michaelis, C., Mitzkus, B., Geirhos, R., Rusak, E., Bringmann, O., Ecker, A. S., Bethge, M., and Brendel, W. (2019). Benchmarking robustness in object detection: Autonomous driving when winter is coming. In *Machine Learning for Autonomous Driving Workshop, NeurIPS 2019*.

Morerio, P., Volpi, R., Ragonesi, R., and Murino, V. (2020). Generative pseudo-label refinement for unsupervised domain adaptation. In *Proceedings of the IEEE/CVF Winter Conference on Applications of Computer Vision*, pages 3130–3139.

Mu, N. and Gilmer, J. (2019). MNIST-C: A robustness benchmark for computer vision. *arXiv preprint arXiv:1906.02337*.

Nado, Z., Padhy, S., Sculley, D., D’Amour, A., Lakshminarayanan, B., and Snoek, J. (2020). Evaluating prediction-time batch normalization for robustness under covariate shift. *arXiv preprint arXiv:2006.10963*.

Naeini, M. P., Cooper, G., and Hauskrecht, M. (2015). Obtaining well calibrated probabilities using Bayesian binning. In *Proceedings of the AAAI Conference on Artificial Intelligence*, volume 29.

Niculescu-Mizil, A. and Caruana, R. (2005). Predicting good probabilities with supervised learning. In *International Conference on Machine Learning*, pages 625–632.

Peng, X., Usman, B., Kaushik, N., Wang, D., Hoffman, J., and Saenko, K. (2018). VISDA: A synthetic-to-real benchmark for visual domain adaptation. In *Proceedings of the IEEE Conference on Computer Vision and Pattern Recognition Workshops*, pages 2021–2026.

Peters, J., Bühlmann, P., and Meinshausen, N. (2016). Causal inference by using invariant prediction: identification and confidence intervals. *Journal of the Royal Statistical Society. Series B (Statistical Methodology)*, pages 947–1012.

Quiñonero-Candela, J., Sugiyama, M., Lawrence, N. D., and Schwaighofer, A. (2009). *Dataset Shift in Machine Learning*. MIT Press.

Recht, B., Roelofs, R., Schmidt, L., and Shankar, V. (2019). Do imagenet classifiers generalize to imagenet? In *International Conference on Machine Learning*, pages 5389–5400.

Roy, P., Ghosh, S., Bhattacharya, S., and Pal, U. (2019). Effects of degradations on deep neural network architectures.

Royer, A. and Lampert, C. (2020). A flexible selection scheme for minimum-effort transfer learning. In *Proceedings of the IEEE/CVF Winter Conference on Applications of Computer Vision*, pages 2191–2200.

Russakovsky, O., Deng, J., Su, H., Krause, J., Satheesh, S., Ma, S., Huang, Z., Karpathy, A., Khosla, A., Bernstein, M., et al. (2015). Imagenet large scale visual recognition challenge. *International Journal of Computer Vision*, 115(3):211–252.

Saenko, K., Kulis, B., Fritz, M., and Darrell, T. (2010). Adapting visual category models to new domains. In *European Conference on Computer Vision*, pages 213–226. Springer.

Schneider, S., Rusak, E., Eck, L., Bringmann, O., Brendel, W., and Bethge, M. (2020). Improving robustness against common corruptions by covariate shift adaptation. In *Advances in Neural Information Processing Systems*, pages 11539–11551.

Shu, R., Bui, H., Narui, H., and Ermon, S. (2018). A DIRT-t approach to unsupervised domain adaptation. In *International Conference on Learning Representations*.

Simard, P., Victorri, B., LeCun, Y., and Denker, J. S. (1991). Tangent prop-a formalism for specifying selected invariances in an adaptive network. In *Advances in Neural Information Processing Systems*, pages 895–903.

Storkey, A. J. (2009). When training and test sets are different: characterising learning transfer. In *Dataset Shift in Machine Learning*, pages 3–28. MIT Press.

Sun, B. and Saenko, K. (2016). Deep coral: Correlation alignment for deep domain adaptation. In *European Conference on Computer Vision*, pages 443–450. Springer.

Sun, Y., Tzeng, E., Darrell, T., and Efros, A. A. (2019). Unsupervised domain adaptation through self-supervision. *arXiv preprint arXiv:1909.11825*.

Torralba, A. and Efros, A. A. (2011). Unbiased look at dataset bias. In *Proceedings of The IEEE Conference on Computer Vision and Pattern Recognition*, pages 1521–1528.

Tzeng, E., Hoffman, J., Saenko, K., and Darrell, T. (2017). Adversarial discriminative domain adaptation. In *Proceedings of the IEEE Conference on Computer Vision and Pattern Recognition*, pages 7167–7176.

Van der Maaten, L. and Hinton, G. (2008). Visualizing data using t-SNE. *Journal of Machine Learning Research*, 9(11).

Volk, G., Müller, S., von Bernuth, A., Hospach, D., and Bringmann, O. (2019). Towards robust CNN-based object detection through augmentation with synthetic rain variations. In *IEEE Intelligent Transportation Systems Conference*, pages 285–292.

Wang, D., Shelhamer, E., Liu, S., Olshausen, B., and Darrell, T. (2021). TENT: Fully test-time adaptation by entropy minimization. In *International Conference on Learning Representations*.

Yang, Y., Morillo, I. G., and Hospedales, T. M. (2018). Deep neural decision trees. In *ICML Workshop on Human Interpretability in Machine Learning (WHI)*.

Yeh, H.-W., Yang, B., Yuen, P. C., and Harada, T. (2021). Sofa: Source-data-free feature alignment for unsupervised domain adaptation. In *Proceedings of the IEEE/CVF Winter Conference on Applications of Computer Vision*, pages 474–483.

Yosinski, J., Clune, J., Bengio, Y., and Lipson, H. (2014). How transferable are features in deep neural networks? In *Advances in Neural Information Processing Systems*, page 3320–3328.

Zadrozny, B. and Elkan, C. (2001). Obtaining calibrated probability estimates from decision trees and naive bayesian classifiers. In *International Conference on Machine Learning*, pages 609–616.

Zech, J. R., Badgeley, M. A., Liu, M., Costa, A. B., Titano, J. J., and Oermann, E. K. (2018). Variable generalization performance of a deep learning model to detect pneumonia in chest radiographs: a cross-sectional study. *PLoS Medicine*, 15(11):e1002683.

Zeiler, M. D. and Fergus, R. (2014). Visualizing and understanding convolutional networks. In *European Conference on Computer Vision*, pages 818–833. Springer.

Zellinger, W., Grubinger, T., Lugoferer, E., Natschläger, T., and Saminger-Platz, S. (2017). Central moment discrepancy (cmd) for domain-invariant representation learning. In *International Conference on Learning Representations*.

A Appendix

A.1 Soft binning

Function. Let $z \sim p_z$ be a continuous 1D variable for which we have n samples $\{z^{(i)}\}_{i=1}^n$. The goal is approximately parameterize p_z using B normalized bin counts $\pi_z = [\pi_{z,1}, \dots, \pi_{z,B}]$, where $\pi_{z,b}$ represents the probability that z falls into bin b and $\sum_{b=1}^B \pi_{z,b} = 1$. We achieve this using the soft binning function of Yang et al. (2018, Section 3.1). The first step is to find the range of z , i.e. the minimum and maximum denoted $z^{min} = \min_i z^{(i)}$ and $z^{max} = \max_i z^{(i)}$ respectively. This will allow us to normalize the range of our samples $z^{(i)}$ to be $[0, 1]$ and thus ensure that binning “softness”, i.e. the degree to which mass is distributed into nearby bins, is comparable across variables with different ranges. The second step is to define $B - 1$ uniformly-spaced and monotonically-increasing cut points (i.e. bin edges) over this normalized range $[0, 1]$, denoted $\mathbf{c} = [c_1, c_2, \dots, c_{B-1}] = \frac{1}{B-2}[0, 1, 2, \dots, B-3, B-2]$. The third step is to compute the B -dimensional vector of soft counts for a sample $z^{(i)}$, denoted $\mathbf{u}(z^{(i)})$, using soft binning vector-valued function \mathbf{u} ,

$$\mathbf{u}(z^{(i)}; z^{min}, z^{max}) = \sigma\left(\left(\frac{z^{(i)} - z^{min}}{z^{max} - z^{min}}\right) + \mathbf{w}_0\right)/\tau, \quad (4)$$

where $\mathbf{w} = [1, 2, \dots, B]$, $\mathbf{w}_0 = [0, -c_1, -c_1 - c_2, \dots, -\sum_{j=1}^{B-1} c_j]$, $\tau > 0$ is a temperature factor, σ is the softmax function, $\mathbf{u}(z^{(i)})_b$ is the mass assigned to bin b , and $\sum_{b=1}^B \mathbf{u}(z^{(i)})_b = 1$. Note that: (i) both \mathbf{w} and \mathbf{w}_0 are constant vectors for a pre-specified number of bins B ; (ii) as $\tau \rightarrow 0$, $\mathbf{u}(z^{(i)})$ tends to a one-hot vector; and (iii) the $B - 1$ cut points \mathbf{c} result in B bins, where values $z^{(i)} < 0$ or $z^{(i)} > 1$ are handled sensibly by the soft binning function in order to catch new samples that lie outside the range of our original n samples (as $\tau \rightarrow 0$, they will appear in the leftmost or rightmost bin respectively). Finally, we get the total counts per bin by summing over the per-sample soft counts $\mathbf{u}(z^{(i)})$, before normalising by the total number of samples n to get the normalized bin counts π_z , i.e., $\pi_z = \sum_{i=1}^n \frac{\mathbf{u}(z^{(i)}; z^{min}, z^{max})}{n}$.

Memory cost. When using 32-bit floating point numbers for each (soft) bin count, the memory cost of soft binning is $32 \times B \times D$ bits—depending only on the number bins B and the number of features D , and *not* on the dataset size. For concreteness, Table 5 compares the cost of storing bin counts to that of: (i) storing the whole source dataset; and (ii) storing the (weights of the) source model. As in our experiments, we assume 8 bins per feature and the following network architectures: a variation of LeNet (LeCun et al., 1998) for MNIST, ResNet-18 (He et al., 2016) for CIFAR-100, and ResNet-101 (He et al., 2016) for both VisDA-C (Peng et al., 2018) and ImageNet (Russakovsky et al., 2015).

Table 5: Storage size for different datasets and their corresponding source models.

Storage size (MB)	MNIST	CFR-100	VisDA-C	ImageNet
Source dataset	33	150	7885	138000
Source model	0.9	49	173	173
Source bin-counts	0.004	0.02	0.5	0.5

A.2 SFDA and related settings

Table 6 compares the setting of SFDA to the related settings of fine-tuning, unsupervised domain adaptation (UDA), and domain generalization (DG).

A.3 FR algorithm

Algorithm 1 gives the algorithm for FR at *development time*, where a source model is trained before saving approximations of the feature and logit distributions under the source data. Algorithm 2 gives the algorithm for FR at *deployment time*, where the feature-extractor is adapted such that the

Table 6: Source-free domain adaptation and related settings. Adapted from Wang et al. (2021).

Setting	Source data	Target data	Adapt. Loss
Fine-tuning	-	x^t, y^t	$L(x^t, y^t)$
UDA	x^s, y^s	x^t	$L(x^s, y^s) + L(x^s, x^t)$
Domain gen.	x^s, y^s	-	$L(x^s, y^s)$
Source-free DA	-	x^t	$L(x^t)$

approximate feature and logit distributions under the target data realign with those saved on the source data.

Algorithm 1: FR at *development* time.

Input: Source model f_s , labelled source data $D_s = (X_s, Y_s)$, number of bins B , number of training iterations I .

```

/* Train source model  $f_s = h \circ g_s$  */
1 for  $i$  in range( $I$ ) do
2    $L_i \leftarrow \mathcal{L}_{src}(f_s, D_s)$  ;
3    $f_s \leftarrow \text{SGD}(f_s, L_i)$  ;
/* Calc. feat. & logit ranges */
4  $\mathbf{z}^{min}, \mathbf{z}^{max} \leftarrow \text{CALC_RANGES}(f_s, X_s)$  ;
5  $\mathbf{a}^{min}, \mathbf{a}^{max} \leftarrow \text{CALC_RANGES}(f_s, X_s)$  ;
/* Calc. feat. & logit bin counts */
6  $\pi_{\mathbf{z}}^s \leftarrow \text{CALC_BC}(f_s, X_s; \mathbf{z}^{min}, \mathbf{z}^{max}, B)$  ;
7  $\pi_{\mathbf{a}}^s \leftarrow \text{CALC_BC}(f_s, X_s; \mathbf{a}^{min}, \mathbf{a}^{max}, B)$  ;
/* Gather source params/stats  $\mathcal{S}^s$  */
8  $\mathcal{S}_s \leftarrow \{\pi_{\mathbf{z}}^s, \pi_{\mathbf{a}}^s, \mathbf{z}^{min}, \mathbf{z}^{max}, \mathbf{a}^{min}, \mathbf{a}^{max}\}$  ;

```

Output: f_s, \mathcal{S}_s

Algorithm 2: FR at *deployment* time.

Input: Source model f_s , unlabelled target data X_t , source data statistics \mathcal{S}_s , number of adaptation iterations I .

```

/* Init target model  $f_t = h \circ g_t$  */
1  $f_t \leftarrow f_s$  ;
/* Adapt target feature-extractor  $g_t$  */
2 for  $i$  in range( $I$ ) do
3    $\pi_{\mathbf{z}}^t \leftarrow \text{CALC_BC}(f_t, X_t; \mathbf{z}^{min}, \mathbf{z}^{max}, B)$  ;
4    $\pi_{\mathbf{a}}^t \leftarrow \text{CALC_BC}(f_t, X_t; \mathbf{a}^{min}, \mathbf{a}^{max}, B)$  ;
5    $L_i \leftarrow \mathcal{L}_{tgt}(\pi_{\mathbf{z}}^s, \pi_{\mathbf{z}}^t, \pi_{\mathbf{a}}^s, \pi_{\mathbf{a}}^t)$  ;
6    $g_t \leftarrow \text{SGD}(g_t, L_i)$  ;

```

Output: g_t

A.4 Further discussion of FR assumptions

A.4.1 When might FR work?

Toy example where FR will work. Let L take two values $\{-1, 1\}$, and let

$$Y = L \tag{5}$$

$$X = U[L - 0.5, L + 0.5] + E, \tag{6}$$

where U denotes a uniform distribution and E a domain-specific offset (this setup of measurement shift is depicted in Figure 1a). Then the optimal classifier $f : X \rightarrow Y$ can be written as $f(X) = \text{sign}(X - E)$. Imagine the source domain has $E = 0$, and the target domain has $E = 2$. Then all points will be initially classified as positive in the target domain, but FR will restore optimal performance by essentially “re-normalizing” X to achieve an intermediate feature representation Z with the same distribution as before (in the source domain).

Toy example where FR will not work. Let L be a rotationally-symmetric multivariate distribution (e.g. a standard multivariate Gaussian), and let X be a rotated version of L where the rotation depends on E . Now let $Y = L_1$, the first component of L . Then any projection of X will have the correct marginal distribution, hence FR will not work here as matching the marginal distributions of the intermediate feature representation Z will not be enough to yield the desired invariant representation.

Common UDA tasks—will FR work? As discussed in Section 2, the assumption of measurement shift tells us that there *exists* a domain-invariant representation that tells us everything we need to know



Figure 5: Domain-shift examples. *Top*: source data. *Bottom*: target data. *Left to right*: EMNIST-DA (‘0’), CIFAR-10-C (‘frog’), VisDA-C (‘person’).

about Y . However, it does *not* tell us whether or not it is possible to extract such a representation from the source domain. For example, in the synthetic-to-real object-recognition task of VisDA-C (Peng et al., 2018), one may hope to discover features in the synthetic domain that capture the geometric aspects of the classes, and then to restore these features in the real domain. However, predictors tend to exploit spurious correlations or “shortcuts” (Arjovsky et al., 2019; Geirhos et al., 2020) in the synthetic domain which are not discriminative in the target domain (perhaps unsurprising given that the person-class contains only 2 synthetic “people”, rendered from different viewpoints with varying lighting, e.g. see top-right picture of Figure 5). As a result, the standard approach for this task is to first pretrain on ImageNet to gain more “general” features and then carefully fine-tune these features on (i) the source domain, and then (ii) the target domain, effectively making the adaptation task ImageNet \rightarrow synthetic \rightarrow real. As adaptation in the target domain relies on recombining these general ImageNet features in a new way, many works seek to improve feature-retention by substantially lowering the learning rate of early layers when learning in the source domain (e.g. Liang et al. 2020). This setup violates the two main assumptions required for FR. Firstly, the assumption of measurement shift is violated—these datasets contain significant label shift, i.e. $E \not\perp\!\!\!\perp Y$. Secondly, it is not possible to learn features in the source domain that, if they can be extracted once more, will discriminate well between the classes in the target domain—as illustrated by the *necessity* of ImageNet pretraining (see Table 7, where all SFDA methods fail without ImageNet pretraining). While we focused on VisDA-C here, the same holds true for other popular UDA tasks like Office (Saenko et al., 2010).

Common UDA tasks—reducing the violation of MS. As discussed in the previous paragraph, VisDA-C contains significant label shift. For example, 8% of examples are labelled ‘car’ in the source domain, while 19% of examples are labelled ‘car’ in the target domain. To correct for this while retaining as many examples as possible, we randomly drop examples from some classes and oversample examples from others so that all classes have 11000 examples in the source domain and 3500 examples in the target domain—this is labelled as “No label shift” in Table 7. In Table 7 we see that: (i) all (tested) SFDA methods fail without ImageNet pre-training—despite similar accuracy being achieved in the source domain with or without ImageNet pre-training (compare \mathbf{XX} vs. $\checkmark\mathbf{X}$); (ii) while FR considerably improves upon AdaBN (Li et al., 2017) with the standard VisDA-C setup (i.e. $\checkmark\mathbf{X}$), it is significantly outperformed by SHOT (Liang et al., 2020) which learns *new* discriminative features in the target domain; and (iii) correcting for label shift boosts the performance of FR, and closes the gap with SHOT (compare $\checkmark\mathbf{X}$ vs. $\checkmark\checkmark$). These results were achieved using a standard VisDA-C implementation/setup: we train a ResNet-101 (He et al., 2016) (optionally pre-trained on ImageNet) for 15 epochs using SGD, a learning rate of 0.001, and a batch size of 64. We additionally adopt the learning rate scheduling of (Ganin and Lempitsky, 2015; Long et al., 2018; Liang et al., 2020) in the source domain, and reduce the learning rate to 0.0001 in the target domain.

Common UDA tasks—summary. Common UDA tasks like VisDA-C and Office require learning *new* discriminative features in the target domain, as illustrated by the necessity of ImageNet pre-training. This is not the *modus operandi* of FR which seeks to extract the *same* features in the target domain. In these setups, other SFDA methods are more suitable, e.g. SHOT (Liang et al., 2020). Figure 5 depicts domain shifts for which FR is suitable (first two columns), and for which FR is not suitable (final column).

Table 7: VisDA-C results (ResNet-101). No corrupt.: accuracy of the source model on the *source data*. No label shift: examples were dropped or oversampled to correct for label shift.

Model	ImageNet pretrain	No label shift	Avg. Acc.
No corrupt.	✗	✗	99.8
Source-only	✗	✗	10.4
AdaBN (Li et al., 2017)	✗	✗	15.9
SHOT (Liang et al., 2020)	✗	✗	17.1
FR	✗	✗	16.8
No corrupt.	✓	✗	99.6
Source-only	✓	✗	47.0
AdaBN (Li et al., 2017)	✓	✗	65.2
SHOT (Liang et al., 2020)	✓	✗	82.9
FR	✓	✗	73.7
No corrupt.	✓	✓	99.7
Source-only	✓	✓	44.6
AdaBN (Li et al., 2017)	✓	✓	68.7
SHOT (Liang et al., 2020)	✓	✓	85.0
FR	✓	✓	82.8

A.5 Datasets

Figures 6, 7, 8 and 9 below show examples from the MNIST-M, MNIST-C, EMNIST-DA and CIFAR datasets respectively.



Figure 6: Top: samples from MNIST. Bottom: samples from MNIST-M.

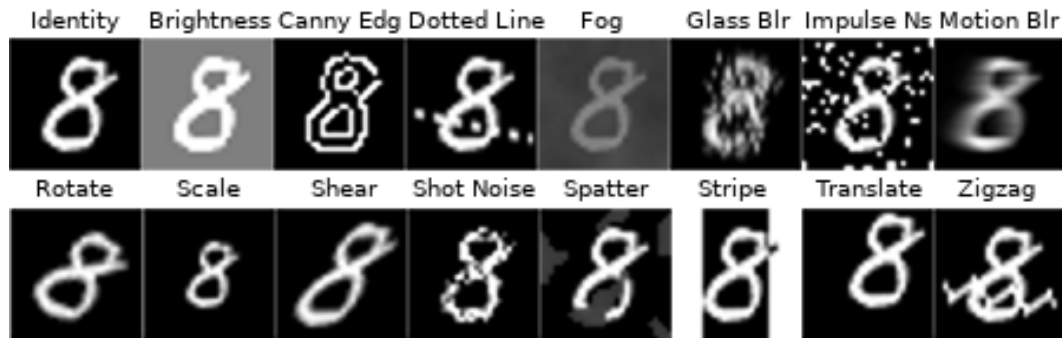


Figure 7: MNIST-C corruptions.

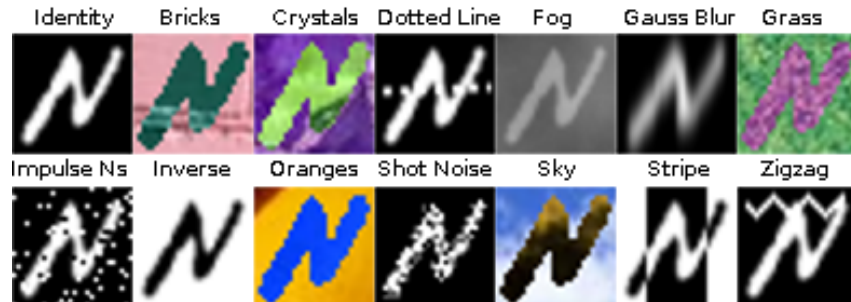


Figure 8: EMNIST-DA corruptions.

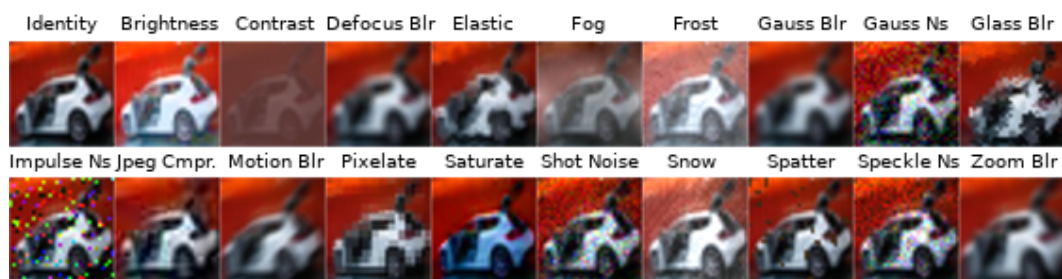


Figure 9: CIFAR corruptions. The same corruptions are used for CIFAR-10-C and CIFAR-100-C.

A.6 Reliability diagrams and confidence histograms

This section shows reliability diagrams (DeGroot and Fienberg, 1983; Niculescu-Mizil and Caruana, 2005) and confidence histograms (Zadrozny and Elkan, 2001): (i) over all EMNIST-DA shifts (see Figure 10); (ii) a severe EMNIST-DA shift (see Figure 11); and (iii) a mild shift EMNIST-DA shift (see Figure 12). Reliability diagrams are given along with the corresponding Expected Calibration Error (ECE, Naeini et al. 2015) and Maximum Calibration Error (MCE, Naeini et al. 2015). ECE is calculated by binning predictions into 10 evenly-spaced bins based on confidence, and then taking a weighted average of the absolute difference between average accuracy and average confidence of the samples in each bin. MCE is the maximum absolute difference between average accuracy and average confidence over the bins. In Figures 10–12 below, we pair each reliability diagram with the corresponding confidence histogram, since reliability diagrams do not provide the underlying frequencies of each bin (as in Guo et al. 2017, Figure 1).

In general we see that most models are overconfident, but our models much less so. As seen by the difference in the size of the red ‘Gap’ bar in the rightmost bins of Figures 10b, 10c, and 10d, when our FR methods predict with high confidence they are much more likely to be correct than IM—a method which works by maximizing prediction confidence. Figure 11 shows that BUFR remains well-calibrated even when the initial shift is severe. Figure 12 shows that, even for a mild shift when all models achieve high accuracy, our methods are better-calibrated. Note that the label ‘Original’ in Figures 10a and 10e denotes the source model on the *source data*, while ‘Source-only’ in Figures 11a, 11e, 12a, and 12e denotes the source model on the *target data*.

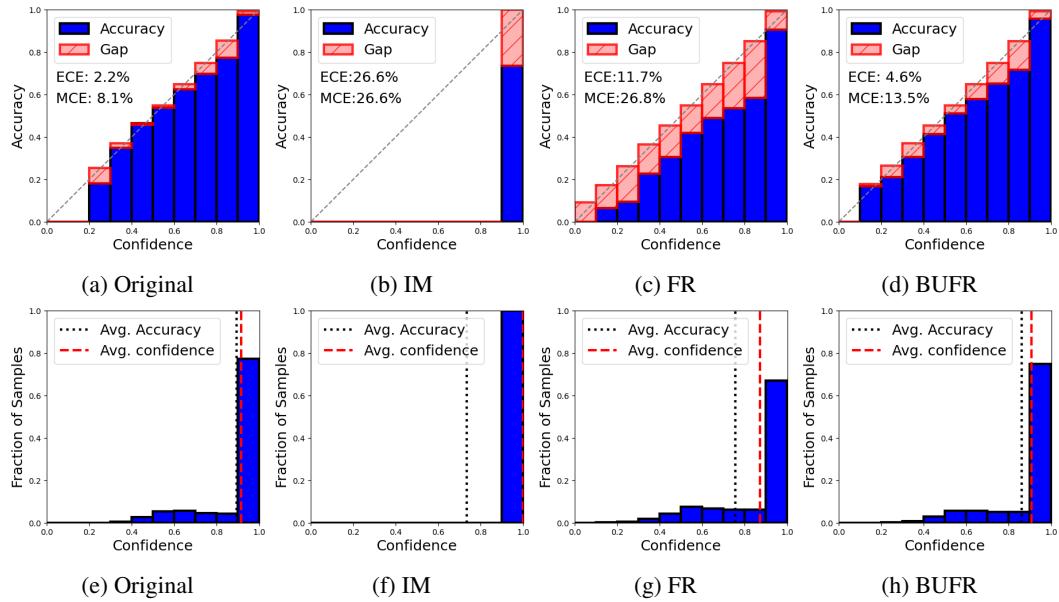


Figure 10: Reliability diagrams and confidence histograms over *all* EMNIST-DA corruptions. (a–d): Reliability diagrams showing the difference between average accuracy and average confidence for different methods. (e–h): Confidence histograms showing the frequency with which predictions are made with a given confidence. Each confidence histogram corresponds with the reliability diagram above it. (a & e): The source model is well-calibrated on the *source data*. (b & f): Entropy minimization leads to extreme overconfidence. (c & g, d & h): Our methods, FR and BUFR, are much better-calibrated as they do not work by making predictions more confident.

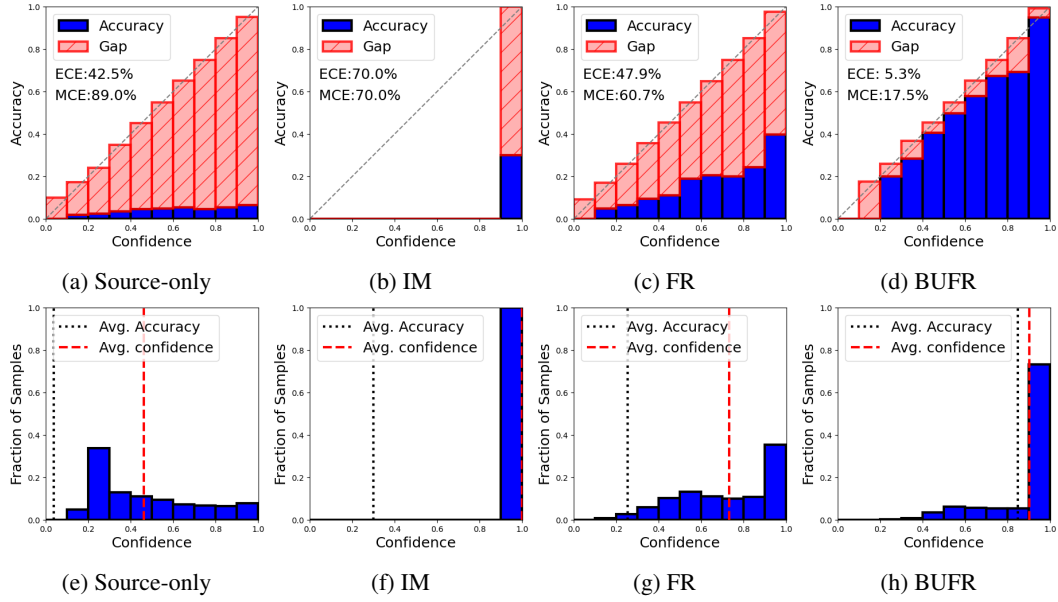


Figure 11: Reliability diagrams and confidence histograms for a severe EMNIST-DA shift (sky) where all methods except BUFR achieve poor accuracy. Each confidence histogram corresponds with the reliability diagram above it. (a & e): Source model on the *target data* achieves poor accuracy and often predicts with low confidence. (b & f): IM also achieves poor accuracy but is highly confident. (d & h): Our BUFR method achieves better ECE and MCE than all other methods.

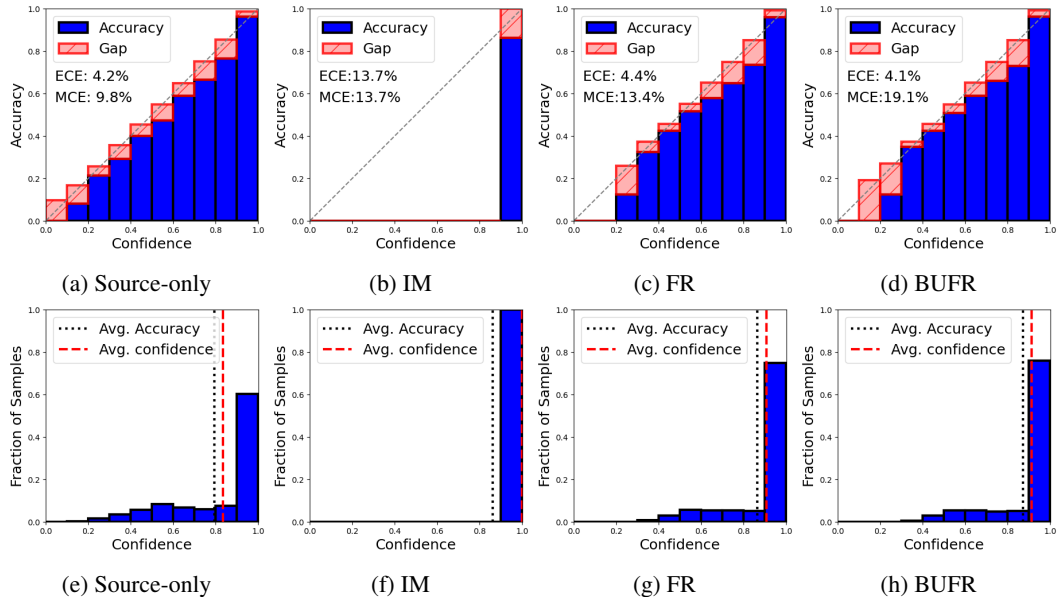


Figure 12: Reliability diagrams and confidence histograms for a mild EMNIST-DA shift (shot noise) where all methods achieve good accuracy. Each confidence histogram corresponds with the reliability diagram above it. When highly confident, our methods (d & h) are more often correct than IM (b & f).

A.7 Activation distributions

EMNIST-DA (skewed). Figure 13 depicts histograms of the marginal feature and logit activation-distributions on the EMNIST-DA stripe shift. As shown, the marginal distributions on the source data (blue curve, those we wish to match) may be heavily-skewed. In contrast, the marginal distributions on the target data (*before adapting*, orange curve) tend to be more symmetric but have a similar mean.

CIFAR (bi-modal). Figure 14 depicts histograms of the marginal feature and logit activation-distributions on the CIFAR-10-C impulse-noise shift. As shown, the marginal distributions on the source data (blue curve, those we wish to match) tend to be bi-modal. In contrast, the marginal distributions on the target data (*before adapting*, orange curve) tend to be uni-modal but have a similar mean. The two modes can be interpreted intuitively as “detected” and “not detected” or “present” and “not present” for a given feature-detector.

Alignment after adapting. Figure 15 shows histograms of the marginal feature activation-distributions on the EMNIST-DA stripe shift. This figure shows curves on the source data (blue curve, same as Figure 13a) and on the target data (*after adapting*, orange curve) for different methods. Evidently, our FR loss causes the marginal distributions to closely align (Figure 15c). In contrast, competing methods (Figures 15a, 15b) do not match the feature activation-distributions, even if they achieve high accuracy. Figure 16 shows the same trend for CIFAR-10-C.

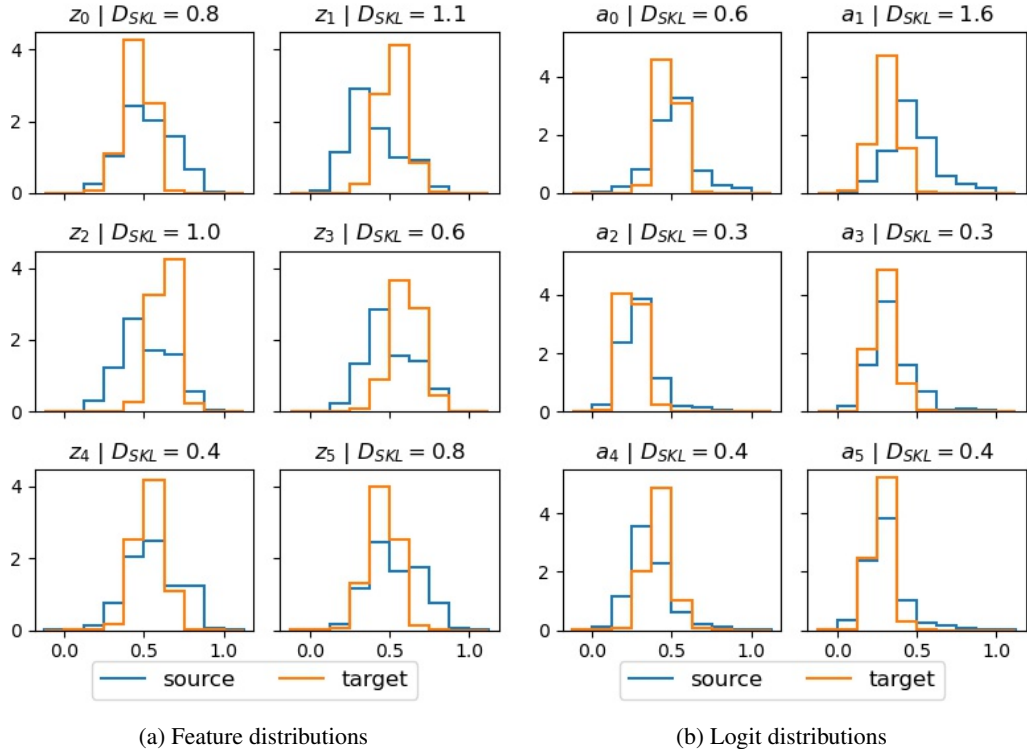


Figure 13: Histograms showing the first 6 marginal activation-distributions on the EMNIST-DA stripe shift. The blue curves are the saved marginal distributions under the source data (i.e. EMNIST). The orange curves are the marginal distributions under the target data *before adaptation* (i.e. the stripe shift). (a) Marginal feature activation-distributions. (b) Marginal logit activation-distributions. D_{SKL} denotes the symmetric KL divergence.

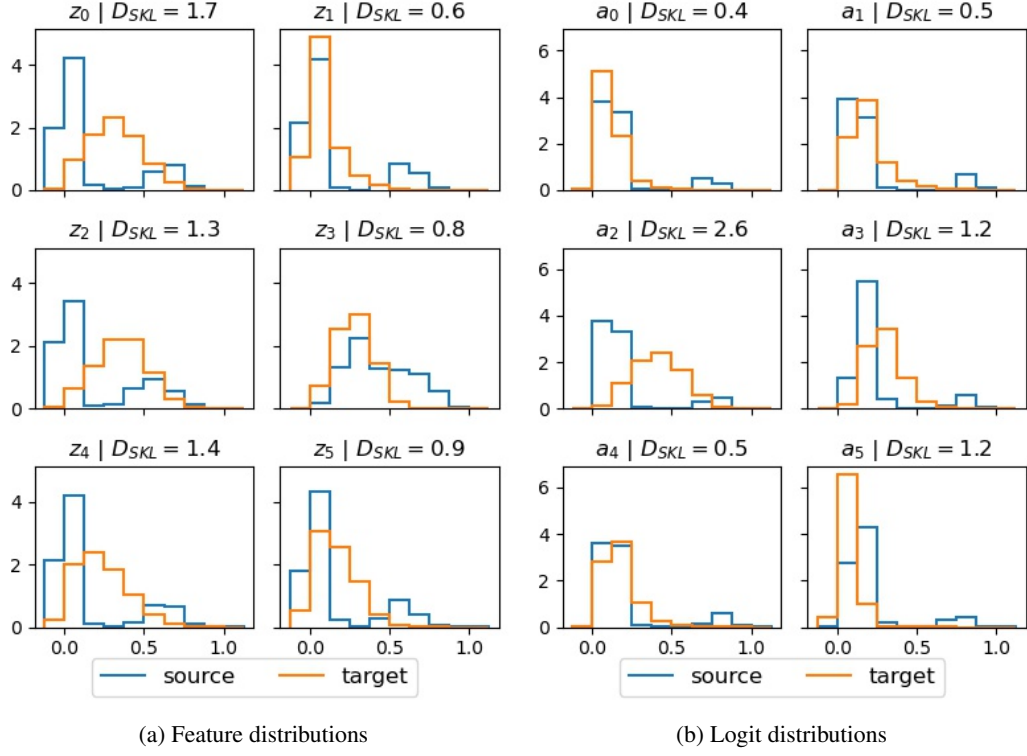


Figure 14: Histograms showing the first 6 marginal activation-distributions on the CIFAR-10-C impulse-noise shift. The blue curves are the saved marginal distributions under the source data (i.e. CIFAR-10). The orange curves are the marginal distributions under the target data *before adaptation* (i.e. the impulse-noise shift). (a) Marginal feature activation-distributions and (b) Marginal logit activation-distributions. D_{SKL} denotes the symmetric KL divergence.

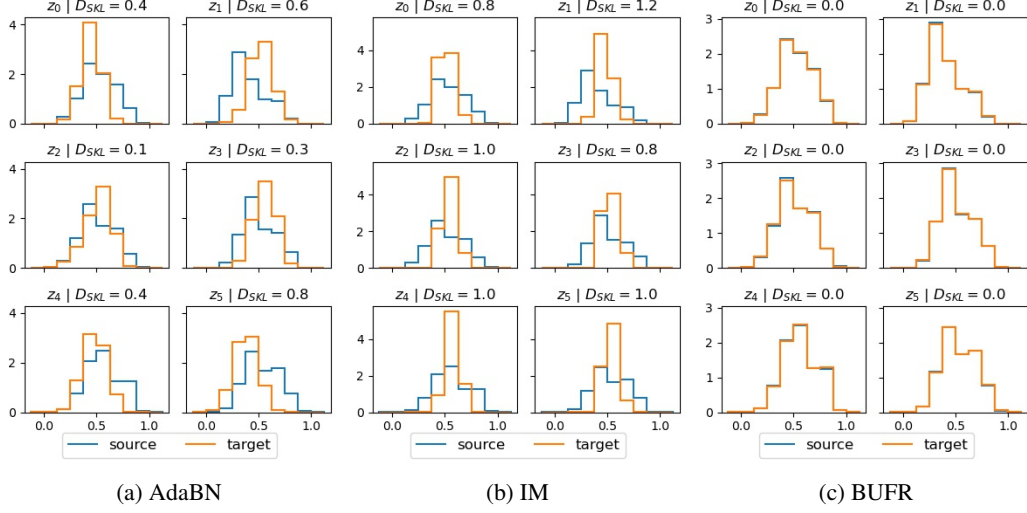


Figure 15: Histograms showing distribution-alignment on the EMNIST-DA stripe shift. The blue curves are the saved marginal distributions under the source data (i.e. EMNIST). The orange curves are the marginal distributions under the target data *after adaptation* (to the stripe shift). (a,b): AdaBN and IM do not align the marginal distributions (despite achieving reasonable accuracy—see Table 12). (c) BUFR matches the activation-distributions very closely, making D_{SKL} very small.

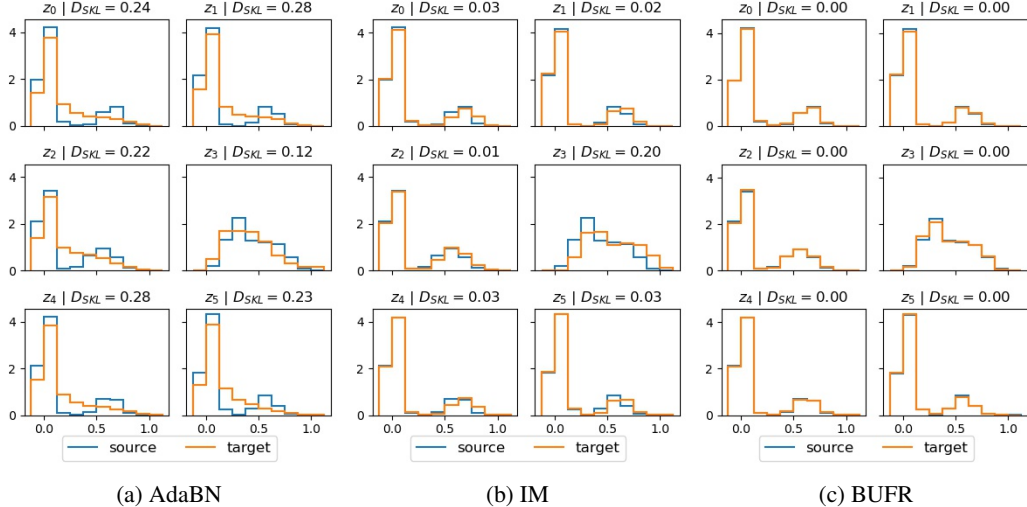


Figure 16: Histograms showing distribution-alignment on the CIFAR-10-C impulse-noise shift. The blue curves are the saved marginal distributions under the source data (i.e. CIFAR-10). The orange curves are the marginal distributions under the target data *after adaptation* (to the impulse-noise shift). (a) AdaBN does not align the marginal distributions. (b) IM only partially-aligns the marginal distributions. (c) BUFR matches the activation-distributions very closely, making D_{SKL} very small.

A.8 Full Results

In this section we give the full results for all datasets and constituent domains.

A.8.1 Digit and character ECEs

Table 8 summarises the ECEs across different models for the digit and character datasets. As discussed in Section 5, our BUFR method outperforms all baseline methods on EMNIST-DA in terms of ECE as it does not work by making predictions more confident.

Table 8: Digit and character ECE (%) results. Shown are the mean and 1 standard deviation. *EMNIST-DA*: mean performance over all 13 EMNIST-DA shifts. *EMNIST-Svr* & *EMNIST-Mld*: sample “severe” and “mild” shifts from EMNIST-DA selected based on AdaBN performance.

Model	MNIST-C	MNIST-M	EMNIST-DA	EMNIST-Svr	EMNIST-Mld
No corrupt.	0.3 ± 0.0	0.3 ± 0.0	2.3 ± 0.1	-	-
Source-only	7.2 ± 1.4	27.0 ± 7.1	30.8 ± 1.6	42.6 ± 3.5	4.8 ± 0.5
AdaBN	4.1 ± 0.1	24.4 ± 2.8	30.3 ± 1.1	52.4 ± 4.9	4.9 ± 0.3
PL	3.1 ± 0.4	56.1 ± 2.2	49.9 ± 0.6	97.2 ± 0.4	16.4 ± 0.1
IM	2.3 ± 0.2	30.9 ± 9.0	29.6 ± 3.7	76.0 ± 7.5	13.7 ± 0.1
SHOT	2.0 ± 0.2	2.8 ± 2.9	19.7 ± 4.4	42.7 ± 23.0	14.8 ± 0.1
FR (ours)	2.5 ± 0.2	9.8 ± 0.8	12.9 ± 0.9	58.0 ± 6.8	4.6 ± 0.3
BUFR (ours)	3.0 ± 0.6	2.9 ± 1.5	4.7 ± 0.2	5.6 ± 0.3	4.2 ± 0.2
Target-superv.	0.5 ± 0.0	1.1 ± 0.1	7.3 ± 0.7	7.0 ± 0.5	8.4 ± 1.1

A.8.2 Online results

We also evaluate our methods in the “online” setting of Wang et al. (2021), where we are restricted to a single pass through the corrupted test data, applying mini-batch updates along the way. As shown in Table 9, FR outperforms existing SFDA methods on CIFAR-10-C in terms of both accuracy and ECE. On CIFAR-100-C, our method is competitive with TENT (Wang et al., 2021)—a method designed specifically for this online setting. As in Wang et al. (2021) these results represent the average over batches *during training* (i.e. a single pass through the test data), rather than the average at the end of training, in order to evaluate *online* performance. We omit BUFR from this table as it is not easily applicable to the online setting—it is difficult to set the number of steps per block without information on the total number of steps/batches (generally not available in an online setting). Full per-shift results for this online setting are given in Tables 18 and 19 for CIFAR-10-C, and Tables 20 and 21 for CIFAR-100-C.

Table 9: Online results. *Left*: Classification accuracy (%). *Right*: Expected Calibration Error (%).

Model	CFR-10-C	CFR-100-C	Model	CFR-10-C	CFR-100-C
AdaBN	80.3 ± 0.0	56.6 ± 0.3	AdaBN	12.1 ± 0.0	10.0 ± 0.1
IM	83.2 ± 0.2	62.3 ± 0.3	IM	10.9 ± 0.1	13.8 ± 0.1
TENT	81.8 ± 0.2	63.1 ± 0.3	TENT	11.5 ± 0.1	14.3 ± 0.1
FR (ours)	85.9 ± 0.3	62.7 ± 0.3	FR (ours)	9.5 ± 0.2	13.6 ± 0.1

A.8.3 MNIST-C full results

Tables 10 and 11 show the accuracy and ECE results for each individual corruption of the MNIST-C dataset. We provide the average performance with and without the translate corruption as the assumptions behind the methods that rely on a fixed classifier h no longer hold. Without the translate corruption (Avg.\translate) we see that all methods achieve high accuracy ($\geq 95\%$).

Table 10: MNIST-C accuracy (%) results. Shown are the mean and 1 standard deviation.

	Src-only	AdaBN	PL	IM	SHOT	FR	BUFR
Brightness	84.8 \pm 11.4	99.4 \pm 0.0	99.5 \pm 0.0	99.4 \pm 0.1	99.5 \pm 0.1	98.7 \pm 0.1	99.2 \pm 0.1
Canny Edges	72.2 \pm 0.8	91.0 \pm 0.7	96.2 \pm 1.0	98.1 \pm 0.1	98.6 \pm 0.1	97.8 \pm 0.1	98.5 \pm 0.0
Dotted Line	98.6 \pm 0.2	98.8 \pm 0.2	99.3 \pm 0.1	99.4 \pm 0.1	99.4 \pm 0.1	98.6 \pm 0.1	99.1 \pm 0.0
Fog	30.1 \pm 12.5	93.9 \pm 1.9	99.3 \pm 0.0	99.4 \pm 0.1	99.5 \pm 0.0	98.6 \pm 0.1	99.2 \pm 0.0
Glass Blur	88.9 \pm 2.3	95.3 \pm 0.3	97.8 \pm 0.1	98.2 \pm 0.1	98.3 \pm 0.0	97.2 \pm 0.1	97.9 \pm 0.0
Impulse Noise	95.2 \pm 0.6	97.9 \pm 0.1	98.4 \pm 0.1	98.7 \pm 0.1	98.9 \pm 0.1	97.8 \pm 0.0	98.6 \pm 0.0
Motion Blur	85.6 \pm 3.9	97.3 \pm 0.4	98.8 \pm 0.1	99.1 \pm 0.1	99.2 \pm 0.1	98.1 \pm 0.1	98.8 \pm 0.1
Rotate	96.7 \pm 0.1	96.7 \pm 0.0	97.7 \pm 0.1	98.4 \pm 0.1	98.8 \pm 0.0	97.5 \pm 0.1	97.9 \pm 0.1
Scale	97.2 \pm 0.1	97.2 \pm 0.1	98.7 \pm 0.1	99.1 \pm 0.0	99.2 \pm 0.0	98.0 \pm 0.0	98.7 \pm 0.2
Shear	98.9 \pm 0.1	98.9 \pm 0.0	99.0 \pm 0.0	99.1 \pm 0.0	99.2 \pm 0.0	98.3 \pm 0.1	98.8 \pm 0.1
Shot Noise	98.6 \pm 0.0	99.0 \pm 0.0	99.2 \pm 0.0	99.2 \pm 0.1	99.2 \pm 0.0	98.3 \pm 0.2	99.0 \pm 0.1
Spatter	98.7 \pm 0.1	98.8 \pm 0.1	99.0 \pm 0.1	99.0 \pm 0.0	99.1 \pm 0.1	98.4 \pm 0.1	98.8 \pm 0.0
Stripe	91.1 \pm 1.2	90.9 \pm 1.5	97.9 \pm 1.0	99.2 \pm 0.0	99.4 \pm 0.1	98.3 \pm 0.1	99.1 \pm 0.1
Translate	64.6 \pm 0.5	64.4 \pm 0.6	69.5 \pm 0.8	75.1 \pm 4.1	78.7 \pm 3.1	76.7 \pm 2.1	64.5 \pm 8.9
Zigzag	91.8 \pm 0.6	93.0 \pm 0.2	98.2 \pm 0.2	98.9 \pm 0.1	99.2 \pm 0.1	98.2 \pm 0.1	98.8 \pm 0.1
Avg.	86.2 \pm 1.8	94.2 \pm 0.2	96.6 \pm 0.1	97.3 \pm 0.2	97.7 \pm 0.2	96.7 \pm 0.1	96.4 \pm 0.6
Avg.\translate	87.7 \pm 1.9	96.3 \pm 0.2	98.5 \pm 0.1	98.9 \pm 0.0	99.1 \pm 0.0	98.1 \pm 0.1	98.7 \pm 0.0

Table 11: MNIST-C ECE (%) results. Shown are the mean and 1 standard deviation.

	Src-only	AdaBN	PL	IM	SHOT	FR	BUFR
Brightness	2.4 \pm 0.4	0.3 \pm 0.1	0.3 \pm 0.1	0.4 \pm 0.1	0.9 \pm 0.1	0.9 \pm 0.1	0.5 \pm 0.1
Canny Edges	22.2 \pm 0.7	6.1 \pm 0.7	4.0 \pm 2.5	1.5 \pm 0.1	0.6 \pm 0.1	1.6 \pm 0.1	1.0 \pm 0.1
Dotted Line	0.7 \pm 0.1	0.7 \pm 0.1	0.5 \pm 0.1	0.4 \pm 0.1	0.9 \pm 0.0	1.0 \pm 0.1	0.6 \pm 0.1
Fog	26.4 \pm 18.0	3.5 \pm 1.4	0.5 \pm 0.0	0.4 \pm 0.0	0.9 \pm 0.1	1.0 \pm 0.1	0.5 \pm 0.1
Glass Blur	5.9 \pm 1.6	3.1 \pm 0.3	1.8 \pm 0.1	1.4 \pm 0.1	0.4 \pm 0.2	2.1 \pm 0.1	1.5 \pm 0.1
Impulse Noise	1.2 \pm 0.2	1.2 \pm 0.1	1.2 \pm 0.1	0.9 \pm 0.1	0.7 \pm 0.1	1.5 \pm 0.1	1.0 \pm 0.1
Motion Blur	9.1 \pm 3.4	1.4 \pm 0.2	1.0 \pm 0.2	0.7 \pm 0.1	0.8 \pm 0.0	1.4 \pm 0.1	0.8 \pm 0.1
Rotate	2.0 \pm 0.1	2.2 \pm 0.1	1.9 \pm 0.1	1.2 \pm 0.1	0.6 \pm 0.1	1.9 \pm 0.1	1.5 \pm 0.1
Scale	1.0 \pm 0.1	1.7 \pm 0.1	1.0 \pm 0.1	0.7 \pm 0.1	0.8 \pm 0.1	1.5 \pm 0.0	0.8 \pm 0.1
Shear	0.7 \pm 0.1	0.7 \pm 0.0	0.8 \pm 0.1	0.7 \pm 0.1	0.8 \pm 0.1	1.2 \pm 0.1	0.9 \pm 0.1
Shot Noise	0.7 \pm 0.1	0.6 \pm 0.1	0.5 \pm 0.1	0.5 \pm 0.1	0.8 \pm 0.1	1.2 \pm 0.1	0.7 \pm 0.1
Spatter	0.6 \pm 0.1	0.7 \pm 0.1	0.7 \pm 0.1	0.7 \pm 0.1	0.9 \pm 0.1	1.2 \pm 0.1	0.8 \pm 0.0
Stripe	4.3 \pm 1.0	6.5 \pm 1.4	2.8 \pm 3.1	0.5 \pm 0.1	0.9 \pm 0.1	1.2 \pm 0.2	0.6 \pm 0.0
Translate	25.2 \pm 0.3	28.6 \pm 0.6	29.0 \pm 0.7	24.2 \pm 4.1	19.2 \pm 3.0	18.8 \pm 2.7	33.7 \pm 8.9
Zigzag	5.4 \pm 0.5	4.9 \pm 0.3	1.3 \pm 0.2	0.8 \pm 0.0	0.8 \pm 0.0	1.4 \pm 0.1	0.8 \pm 0.1
Avg.	7.2 \pm 1.4	4.1 \pm 0.1	3.1 \pm 0.4	2.3 \pm 0.2	2.0 \pm 0.2	2.5 \pm 0.2	3.0 \pm 0.6
Avg.\translate	5.9 \pm 1.5	2.4 \pm 0.2	1.3 \pm 0.4	0.8 \pm 0.0	0.8 \pm 0.0	1.4 \pm 0.0	0.8 \pm 0.0

A.8.4 EMNIST-DA full results

Tables 12 and 13 show the accuracy and ECE results for each individual shift of EMNIST-DA. We provide the average performance with and without the ‘background shifts’ (bgs), where the background and digit change colour, as these are often the most severe shifts.

Table 12: EMNIST-DA accuracy (%) results. Shown are the mean and 1 standard deviation.

	Src-only	AdaBN	PL	IM	SHOT	FR	BUFR
Bricks	4.2 \pm 0.5	5.9 \pm 1.0	6.8 \pm 1.2	20.5 \pm 4.8	76.0 \pm 0.2	32.4 \pm 4.8	83.8 \pm 0.3
Crystals	19.7 \pm 3.1	42.1 \pm 1.9	47.4 \pm 1.6	71.5 \pm 3.8	80.1 \pm 0.2	76.8 \pm 0.4	82.6 \pm 0.3
Dotted Line	76.2 \pm 0.7	80.8 \pm 0.4	80.7 \pm 0.5	87.1 \pm 0.1	87.5 \pm 0.1	87.6 \pm 0.1	88.3 \pm 0.0
Fog	4.5 \pm 0.9	69.0 \pm 2.6	77.4 \pm 3.3	86.2 \pm 0.1	87.0 \pm 0.1	87.0 \pm 0.1	88.3 \pm 0.1
Gaussian Blur	45.1 \pm 3.2	65.2 \pm 1.6	78.8 \pm 0.8	83.7 \pm 0.2	83.9 \pm 0.2	83.0 \pm 0.4	86.0 \pm 0.1
Grass	2.3 \pm 0.1	6.1 \pm 0.4	6.7 \pm 1.8	42.4 \pm 40.9	61.8 \pm 36.5	79.2 \pm 0.3	84.5 \pm 0.2
Impulse Noise	36.8 \pm 1.6	76.7 \pm 0.8	79.9 \pm 0.6	84.4 \pm 0.2	84.4 \pm 0.2	84.8 \pm 0.2	86.0 \pm 0.1
Inverse	5.6 \pm 0.5	8.1 \pm 2.1	11.3 \pm 2.0	83.2 \pm 0.4	85.1 \pm 0.2	83.1 \pm 0.7	88.3 \pm 0.1
Oranges	26.5 \pm 2.7	40.7 \pm 2.3	43.0 \pm 3.1	80.5 \pm 0.3	82.4 \pm 0.2	82.3 \pm 0.3	84.8 \pm 0.3
Shot Noise	78.5 \pm 0.7	84.9 \pm 0.2	85.0 \pm 0.3	86.3 \pm 0.1	86.1 \pm 0.1	86.4 \pm 0.1	87.0 \pm 0.2
Sky	3.8 \pm 0.4	3.7 \pm 0.7	3.3 \pm 0.6	24.0 \pm 7.5	55.1 \pm 23.5	15.3 \pm 6.8	84.6 \pm 0.2
Stripe	15.4 \pm 1.1	46.9 \pm 4.9	63.8 \pm 3.7	83.9 \pm 0.3	85.1 \pm 0.2	84.5 \pm 0.4	87.1 \pm 0.1
Zigzag	65.0 \pm 0.2	71.3 \pm 0.2	72.3 \pm 0.2	81.0 \pm 0.5	85.8 \pm 0.2	85.7 \pm 0.2	87.5 \pm 0.2
Avg.	29.5 \pm 0.5	46.2 \pm 1.1	50.5 \pm 0.6	70.3 \pm 3.7	80.0 \pm 4.4	74.4 \pm 0.8	86.1 \pm 0.1
Avg.\bgs	40.9 \pm 0.4	62.8 \pm 1.1	68.6 \pm 0.5	84.5 \pm 0.1	85.6 \pm 0.1	85.2 \pm 0.1	87.3 \pm 0.0

Table 13: EMNIST-DA ECE (%) results. Shown are the mean and 1 standard deviation.

	Src-only	AdaBN	PL	IM	SHOT	FR	BUFR
Bricks	54.6 \pm 5.0	64.4 \pm 1.1	93.2 \pm 1.2	79.4 \pm 4.8	22.5 \pm 0.3	44.1 \pm 4.2	6.2 \pm 0.4
Crystals	27.0 \pm 3.0	29.0 \pm 1.2	52.7 \pm 1.7	28.5 \pm 3.8	19.3 \pm 0.1	10.5 \pm 0.3	6.9 \pm 0.3
Dotted Line	11.4 \pm 0.6	9.2 \pm 0.5	19.6 \pm 0.7	12.9 \pm 0.1	12.9 \pm 0.1	3.8 \pm 0.2	3.4 \pm 0.2
Fog	19.2 \pm 6.5	13.8 \pm 1.5	24.1 \pm 4.0	13.8 \pm 0.1	13.5 \pm 0.1	3.9 \pm 0.2	3.3 \pm 0.1
Gaussian Blur	15.0 \pm 3.9	15.3 \pm 0.9	21.2 \pm 0.8	16.4 \pm 0.2	16.0 \pm 0.3	6.4 \pm 0.7	4.9 \pm 0.1
Grass	21.6 \pm 5.4	61.3 \pm 0.8	93.6 \pm 1.5	57.5 \pm 40.9	37.5 \pm 36.1	8.7 \pm 0.6	5.7 \pm 0.2
Impulse Noise	32.0 \pm 1.8	9.9 \pm 0.6	20.1 \pm 0.6	15.6 \pm 0.2	15.8 \pm 0.2	5.3 \pm 0.1	4.7 \pm 0.1
Inverse	65.1 \pm 5.8	60.8 \pm 2.2	89.3 \pm 2.1	16.9 \pm 0.5	14.7 \pm 0.1	5.6 \pm 0.5	3.3 \pm 0.1
Oranges	23.8 \pm 2.7	25.3 \pm 2.0	57.6 \pm 2.7	19.6 \pm 0.4	17.4 \pm 0.2	6.9 \pm 0.5	5.5 \pm 0.3
Shot Noise	4.8 \pm 0.5	4.9 \pm 0.3	16.4 \pm 0.1	13.7 \pm 0.1	14.8 \pm 0.1	4.6 \pm 0.3	4.2 \pm 0.2
Sky	42.6 \pm 3.5	52.4 \pm 4.9	97.2 \pm 0.4	76.0 \pm 7.5	42.7 \pm 23.0	58.0 \pm 6.8	5.6 \pm 0.3
Stripe	63.8 \pm 3.0	31.6 \pm 4.4	36.2 \pm 3.8	16.1 \pm 0.3	15.0 \pm 0.3	5.4 \pm 0.2	4.1 \pm 0.1
Zigzag	19.9 \pm 0.3	16.7 \pm 0.2	27.6 \pm 0.2	19.0 \pm 0.5	14.4 \pm 0.1	4.9 \pm 0.1	3.8 \pm 0.2
Avg.	30.8 \pm 1.6	30.3 \pm 1.1	49.9 \pm 0.6	29.6 \pm 3.7	19.7 \pm 4.4	12.9 \pm 0.9	4.7 \pm 0.2
Avg.\bgs	28.9 \pm 1.3	20.3 \pm 0.8	31.8 \pm 0.5	15.6 \pm 0.1	14.6 \pm 0.1	5.0 \pm 0.2	4.0 \pm 0.1

A.8.5 CIFAR-10-C full results

Tables 14 and 15 show the accuracy and ECE results for each individual corruption of CIFAR-10-C. It is worth noting that BUFR achieves the biggest wins on the most severe shifts, i.e. those on which AdaBN (Li et al., 2017) performs poorly.

Table 14: CIFAR-10-C accuracy (%) results. Shown are the mean and 1 standard deviation.

	Src-only	AdaBN	PL	IM	TENT	FR	BUFR
Brightness	91.4 \pm 0.4	91.5 \pm 0.3	91.9 \pm 0.2	92.7 \pm 0.3	93.2 \pm 0.3	93 \pm 0.4	93.3 \pm 0.3
Contrast	32.3 \pm 1.3	87.1 \pm 0.3	86.6 \pm 3.2	90.8 \pm 0.9	91.3 \pm 1.7	90.9 \pm 0.9	92.9 \pm 0.7
Defocus blr	53.1 \pm 6.4	88.8 \pm 0.4	89.3 \pm 0.5	90.5 \pm 0.4	90.9 \pm 0.5	90.9 \pm 0.3	91.5 \pm 0.5
Elastic	77.6 \pm 0.6	78.2 \pm 0.4	79.2 \pm 0.8	81.4 \pm 0.5	82.7 \pm 0.5	82.7 \pm 0.4	84.2 \pm 0.3
Fog	72.9 \pm 2.6	85.9 \pm 0.9	86.5 \pm 0.8	88.7 \pm 0.4	89.5 \pm 0.4	89.5 \pm 0.5	91.5 \pm 0.5
Frost	64.4 \pm 2.4	80.7 \pm 0.7	82.4 \pm 1.2	85.4 \pm 0.6	86.8 \pm 0.7	87 \pm 0.6	89.1 \pm 0.9
Gauss. blr	35.9 \pm 8	88.2 \pm 0.6	89 \pm 0.7	90.5 \pm 0.5	91 \pm 0.6	91.2 \pm 0.6	92.3 \pm 0.4
Gauss. nse	27.7 \pm 5.1	69.2 \pm 1	74.6 \pm 0.6	79.2 \pm 0.9	81.3 \pm 0.5	81.9 \pm 0.1	85.9 \pm 0.4
Glass blr	51.3 \pm 1.8	66.7 \pm 0.4	69 \pm 0.3	73.7 \pm 1	74.7 \pm 0.8	76.8 \pm 0.8	80.3 \pm 0.5
Impulse nse	25.9 \pm 3.8	62.1 \pm 1	67.2 \pm 0.5	73.2 \pm 0.8	75.3 \pm 0.8	76.6 \pm 0.4	89.3 \pm 1.4
Jpeg compr.	74.9 \pm 1	74.1 \pm 1	77.3 \pm 0.6	81 \pm 0.3	82.9 \pm 0.5	83.4 \pm 0.5	85.8 \pm 0.6
Motion blr	66.1 \pm 1.7	87.2 \pm 0.2	87.8 \pm 0.2	89.1 \pm 0.2	90 \pm 0.3	89.8 \pm 0.2	90.8 \pm 0.2
Pixelate	48.2 \pm 2.2	80.4 \pm 0.5	82 \pm 0.4	85.5 \pm 0.7	87.6 \pm 0.9	87.5 \pm 0.8	89.9 \pm 0.6
Saturate	89.9 \pm 0.4	92 \pm 0.1	92.5 \pm 0.3	93.1 \pm 0.1	93.3 \pm 0.1	93.4 \pm 0.4	93.5 \pm 0.3
Shot nse	34.4 \pm 4.9	71.2 \pm 1.2	77.1 \pm 0.9	81.6 \pm 0.7	83.5 \pm 0.6	85.6 \pm 1.9	87 \pm 0.2
Snow	76.6 \pm 1.1	82.4 \pm 0.6	83.8 \pm 1.1	86.4 \pm 0.6	87.8 \pm 0.7	88.4 \pm 1.7	89.7 \pm 0.5
Spatter	75 \pm 0.8	83.3 \pm 0.5	85.5 \pm 0.3	88 \pm 0.2	88.5 \pm 0.3	91 \pm 2.4	92.6 \pm 0.5
Speckle nse	40.7 \pm 3.7	70.4 \pm 0.8	76.1 \pm 1.2	81.3 \pm 1	83.2 \pm 0.9	85.8 \pm 1.7	87.4 \pm 0.4
Zoom blr	60.5 \pm 5.1	88.1 \pm 0.3	89 \pm 0.4	90.6 \pm 0.2	91.3 \pm 0.3	91.2 \pm 0.7	91.6 \pm 0.2
Avg.	57.8 \pm 0.7	80.4 \pm 0.1	82.5 \pm 0.3	85.4 \pm 0.2	86.6 \pm 0.3	87.2 \pm 0.7	89.4 \pm 0.2

Table 15: CIFAR-10-C ECE (%) results. Shown are the mean and 1 standard deviation.

	Src-only	AdaBN	PL	IM	TENT	FR	BUFR
Brightness	4.7 \pm 0.2	4 \pm 0.1	8.1 \pm 0.2	7.2 \pm 0.4	6.4 \pm 0.3	5.9 \pm 0.3	6.2 \pm 0.2
Contrast	43.5 \pm 2.8	5.7 \pm 0.4	13.2 \pm 3.1	9.8 \pm 0.9	8.4 \pm 1.6	6.6 \pm 0.4	6.6 \pm 0.7
Defocus blr	28.2 \pm 4	6.1 \pm 0.4	10.7 \pm 0.5	9.4 \pm 0.4	8.6 \pm 0.5	7.8 \pm 0.3	7.9 \pm 0.4
Elastic	12.4 \pm 0.7	12.6 \pm 0.4	20.8 \pm 0.8	18.6 \pm 0.5	16.5 \pm 0.5	15.1 \pm 0.5	15.2 \pm 0.3
Fog	17.4 \pm 2.1	7.5 \pm 0.7	13.5 \pm 0.8	11.3 \pm 0.3	10.1 \pm 0.4	8.9 \pm 0.3	8 \pm 0.5
Frost	22.7 \pm 1.7	10.4 \pm 0.6	17.5 \pm 1.2	14.6 \pm 0.6	12.7 \pm 0.6	10.7 \pm 0.8	10.3 \pm 0.9
Gauss. blr	40.7 \pm 6.2	6.1 \pm 0.4	11 \pm 0.7	9.5 \pm 0.4	8.5 \pm 0.5	7.5 \pm 0.4	7.3 \pm 0.4
Gauss. nse	57.6 \pm 6.7	18.5 \pm 0.7	25.3 \pm 0.6	20.9 \pm 0.9	18 \pm 0.4	15.9 \pm 0.3	13.3 \pm 0.4
Glass blr	31.2 \pm 1.3	20.8 \pm 0.4	30.9 \pm 0.3	26.3 \pm 1	24.2 \pm 0.8	20.9 \pm 0.7	18.9 \pm 0.5
Impulse nse	51.2 \pm 4	23.3 \pm 0.8	32.7 \pm 0.5	26.8 \pm 0.9	23.7 \pm 0.8	20.6 \pm 0.5	10.2 \pm 1.3
Jpeg compr.	14.6 \pm 0.8	15.5 \pm 0.7	22.6 \pm 0.6	18.9 \pm 0.4	16.4 \pm 0.5	14.5 \pm 0.4	13.6 \pm 0.7
Motion blr	21.1 \pm 1.3	6.8 \pm 0.3	12.1 \pm 0.2	10.9 \pm 0.2	9.5 \pm 0.3	8.7 \pm 0.3	8.6 \pm 0.2
Pixelate	36.9 \pm 2.5	11.1 \pm 0.4	17.9 \pm 0.4	14.5 \pm 0.7	11.9 \pm 0.9	10.7 \pm 0.7	9.5 \pm 0.6
Saturate	5.5 \pm 0.3	4.2 \pm 0.1	7.4 \pm 0.3	6.9 \pm 0.1	6.4 \pm 0.1	5.9 \pm 0.2	6 \pm 0.3
Shot nse	50.2 \pm 5.9	17 \pm 0.9	22.8 \pm 0.9	18.4 \pm 0.7	15.9 \pm 0.6	14 \pm 0.3	12.3 \pm 0.2
Snow	14.3 \pm 0.5	9.8 \pm 0.4	16.1 \pm 1.1	13.6 \pm 0.6	11.6 \pm 0.7	10.5 \pm 0.7	9.7 \pm 0.4
Spatter	16.9 \pm 0.8	9.3 \pm 0.3	14.5 \pm 0.3	12 \pm 0.2	11 \pm 0.2	9.3 \pm 0.2	7 \pm 0.6
Speckle nse	43.2 \pm 4.5	17.9 \pm 0.5	23.8 \pm 1.1	18.7 \pm 1	16.1 \pm 0.9	13.9 \pm 0.7	11.9 \pm 0.4
Zoom blr	24.4 \pm 3.5	6.2 \pm 0.1	11 \pm 0.4	9.4 \pm 0.2	8.3 \pm 0.3	7.6 \pm 0.5	7.9 \pm 0.2
Avg.	28.2 \pm 0.4	11.2 \pm 0.1	17.5 \pm 0.3	14.6 \pm 0.2	12.8 \pm 0.3	11.3 \pm 0.3	10 \pm 0.2

A.8.6 CIFAR-100-C full results

Tables 16 and 17 show the accuracy and ECE results for each individual corruption of CIFAR-100-C. It is worth noting that BUFR achieves the biggest wins on the most severe shifts, i.e. those on which AdaBN (Li et al., 2017) performs poorly.

Table 16: CIFAR-100-C accuracy (%) results. Shown are the mean and 1 standard deviation.

	Src-only	AdaBN	PL	IM	TENT	FR	BUFR
Brightness	63.2 \pm 1.1	66.1 \pm 0.5	69.6 \pm 0.7	72.6 \pm 0.6	72.2 \pm 0.5	71.8 \pm 0.5	73.6 \pm 0.2
Contrast	13.9 \pm 0.6	61.4 \pm 0.4	59.2 \pm 3.5	70.1 \pm 0.4	64 \pm 3.1	68 \pm 0.5	72.2 \pm 0.5
Defocus blr	35.9 \pm 0.7	65.6 \pm 0.1	69.3 \pm 0.1	71.8 \pm 0.3	71 \pm 0.5	71.2 \pm 0.1	72.2 \pm 0.2
Elastic	58.5 \pm 0.7	60.4 \pm 0.2	63.9 \pm 0.4	66.9 \pm 0.2	65.5 \pm 0.2	65.9 \pm 0.4	67.1 \pm 0.5
Fog	36.9 \pm 0.5	55.4 \pm 0.6	60.4 \pm 0.6	66.5 \pm 0.6	67.1 \pm 0.6	64.9 \pm 0.4	70.1 \pm 0.5
Frost	41.1 \pm 0.9	55.3 \pm 0.6	60.1 \pm 0.8	65.2 \pm 0.4	65.3 \pm 0.9	63 \pm 0.5	67.5 \pm 0.7
Gauss. blr	28.2 \pm 1	64.3 \pm 0.3	68.9 \pm 0.1	71.7 \pm 0.2	71 \pm 0.3	70.9 \pm 0.3	72.9 \pm 0.6
Gauss. nse	11.9 \pm 1.2	43.8 \pm 0.6	53.1 \pm 0.7	60.3 \pm 0.4	59.5 \pm 0.6	57.7 \pm 0.4	63 \pm 0.3
Glass blr	45.1 \pm 0.9	53.3 \pm 0.6	57.3 \pm 0.7	62.4 \pm 0.3	61.4 \pm 0.5	60.5 \pm 0.3	63.2 \pm 0.4
Impulse nse	7.2 \pm 0.8	40.8 \pm 0.4	50.6 \pm 0.5	58.4 \pm 0.6	56.3 \pm 0.7	55.2 \pm 0.9	66.9 \pm 0.6
Jpeg compr.	48.6 \pm 0.9	49.8 \pm 0.7	55.8 \pm 0.3	61.2 \pm 0.5	60.8 \pm 0.1	59.3 \pm 0.5	62.6 \pm 0.4
Motion blr	45.1 \pm 0.5	63.4 \pm 0.2	66.3 \pm 0.6	69.7 \pm 0.2	69 \pm 0.5	68.6 \pm 0.4	70.8 \pm 0.2
Pixelate	22.3 \pm 0.4	59.4 \pm 0.6	64.9 \pm 0.6	69.7 \pm 0.4	69.8 \pm 0.4	68.1 \pm 0.3	71.4 \pm 0.5
Saturate	55.8 \pm 0.4	65.7 \pm 0.4	70.2 \pm 0.8	72.6 \pm 0.2	71.4 \pm 0.7	72.2 \pm 0.5	72.4 \pm 0.6
Shot nse	14.1 \pm 1.2	44.6 \pm 0.9	56.1 \pm 0.8	61.9 \pm 0.6	60.3 \pm 0.4	59.8 \pm 0.3	62.1 \pm 2.8
Snow	49.4 \pm 0.8	53.5 \pm 0.4	59.8 \pm 0.9	65 \pm 0.6	65.6 \pm 0.4	63.8 \pm 0.6	65.9 \pm 2.2
Spatter	54.8 \pm 1.1	64.9 \pm 0.6	72.1 \pm 0.3	73.8 \pm 0.4	72.9 \pm 0.5	73.8 \pm 0.5	74.3 \pm 0.2
Speckle nse	15.6 \pm 1.3	42.3 \pm 1	54.2 \pm 1.5	62.1 \pm 0.6	59.8 \pm 0.3	59.6 \pm 0.8	62.1 \pm 2.7
Zoom blr	45.1 \pm 0.7	65.9 \pm 0.3	69.1 \pm 0.5	71.9 \pm 0.3	71.1 \pm 0.8	71 \pm 0.6	71.2 \pm 0.4
Avg.	36.4 \pm 0.5	56.6 \pm 0.3	62.1 \pm 0.2	67 \pm 0.2	66 \pm 0.4	65.5 \pm 0.2	68.5 \pm 0.2

Table 17: CIFAR-100-C ECE (%) results. Shown are the mean and 1 standard deviation.

	Src-only	AdaBN	PL	IM	TENT	FR	BUFR
Brightness	6.3 \pm 0.3	9.4 \pm 0.3	30.2 \pm 0.7	27.4 \pm 0.4	20.7 \pm 0.4	12.4 \pm 0.3	12 \pm 0.6
Contrast	37.8 \pm 2.2	11.4 \pm 0.3	40.5 \pm 3.4	29.6 \pm 0.8	29.5 \pm 3.5	14 \pm 0.2	12.8 \pm 0.5
Defocus blr	16 \pm 0.8	9.7 \pm 0.3	30.6 \pm 0.2	28.2 \pm 0.4	21.6 \pm 0.3	13.4 \pm 0.3	12.7 \pm 0.2
Elastic	8 \pm 0.1	10.8 \pm 0.2	35.9 \pm 0.4	33 \pm 0.3	25.8 \pm 0.1	15.2 \pm 0.2	15.3 \pm 0.3
Fog	21 \pm 0.6	12.2 \pm 0.3	39.5 \pm 0.6	33.3 \pm 0.7	24.8 \pm 0.5	15.9 \pm 0.3	14 \pm 0.6
Frost	14.1 \pm 1.1	13.3 \pm 0.4	39.7 \pm 0.8	34.8 \pm 0.4	26.1 \pm 0.7	16.3 \pm 0.3	15.3 \pm 0.2
Gauss. blr	20.5 \pm 1.4	10 \pm 0.4	31 \pm 0.1	28.4 \pm 0.2	21.7 \pm 0.2	13.5 \pm 0.2	12.5 \pm 0.3
Gauss. nse	39.3 \pm 5.5	16.7 \pm 0.2	46.8 \pm 0.6	39.8 \pm 0.5	30.8 \pm 0.7	19.4 \pm 0.5	17.5 \pm 0.5
Glass blr	15.7 \pm 1.1	13.4 \pm 0.1	42.5 \pm 0.7	37.6 \pm 0.3	29.1 \pm 0.4	17.9 \pm 0.4	17.6 \pm 0.6
Impulse nse	35.1 \pm 2.6	17.4 \pm 0.2	49.3 \pm 0.6	41.5 \pm 0.7	33.7 \pm 0.8	20.5 \pm 0.3	15.2 \pm 0.2
Jpeg compr.	8.6 \pm 0.2	15 \pm 0.4	44.1 \pm 0.4	38.8 \pm 0.5	29.6 \pm 0.2	19.1 \pm 0.2	18.2 \pm 0.5
Motion blr	12.2 \pm 0.2	10.4 \pm 0.3	33.6 \pm 0.6	30.3 \pm 0.2	23.2 \pm 0.4	14.3 \pm 0.3	13.6 \pm 0.3
Pixelate	27.5 \pm 1	11.6 \pm 0.4	35 \pm 0.6	30.3 \pm 0.4	22.5 \pm 0.3	14.2 \pm 0.4	13.6 \pm 0.4
Saturate	8.8 \pm 0.2	9.5 \pm 0.3	29.6 \pm 0.8	27.4 \pm 0.3	21.2 \pm 0.6	12.7 \pm 0.2	12.3 \pm 0.7
Shot nse	37.2 \pm 5.9	16 \pm 0.2	43.7 \pm 0.8	38.1 \pm 0.5	30.2 \pm 0.8	18.6 \pm 0.4	17 \pm 0.6
Snow	8.5 \pm 0.3	14.4 \pm 0.2	40.1 \pm 0.9	34.9 \pm 0.7	25.7 \pm 0.5	17 \pm 0.5	14.9 \pm 0.1
Spatter	6.7 \pm 0.3	9.3 \pm 0.1	27.8 \pm 0.3	26.2 \pm 0.4	20 \pm 0.6	12 \pm 0.3	11 \pm 0.4
Speckle nse	34.5 \pm 5.4	17.2 \pm 0.3	45.7 \pm 1.6	37.9 \pm 0.6	30.6 \pm 0.2	18.7 \pm 0.6	16.8 \pm 0.8
Zoom blr	10.5 \pm 0.3	9.1 \pm 0.2	30.8 \pm 0.5	28.2 \pm 0.4	21.5 \pm 0.7	13.1 \pm 0.5	13.2 \pm 0.7
Avg.	19.4 \pm 0.9	12.5 \pm 0.1	37.7 \pm 0.2	32.9 \pm 0.2	25.7 \pm 0.4	15.7 \pm 0.1	14.5 \pm 0.3

A.8.7 CIFAR-10-C full online results

Tables 18 and 19 show the accuracy and ECE results for each individual corruption of CIFAR-10-C when adapting in an *online* fashion (see Appendix A.8.2). It is worth noting that FR achieves the biggest wins on the most severe shifts, i.e. those on which AdaBN (Li et al., 2017) performs poorly.

Table 18: CIFAR-10-C *online* accuracy (%) results. Shown are the mean and 1 standard deviation.

	Src-only	AdaBN	IM	TENT	FR
Brightness	91.4 \pm 0.4	91.6 \pm 0.2	92.2 \pm 0.4	91.8 \pm 0.3	92.8 \pm 0.3
Contrast	32.3 \pm 1.3	87.1 \pm 0.4	87.8 \pm 0.5	87.8 \pm 0.6	89.8 \pm 0.6
Defocus blr	53.1 \pm 6.4	88.7 \pm 0.5	89.7 \pm 0.5	89.1 \pm 0.5	90.6 \pm 0.5
Elastic	77.6 \pm 0.6	78 \pm 0.3	80.3 \pm 0.6	79.2 \pm 0.5	82 \pm 0.4
Fog	72.9 \pm 2.6	85.9 \pm 1.1	87.2 \pm 0.5	86.5 \pm 0.8	89 \pm 0.8
Frost	64.4 \pm 2.4	80.7 \pm 0.8	83 \pm 0.8	81.8 \pm 0.8	85.9 \pm 0.7
Gauss. blr	35.9 \pm 8	88.3 \pm 0.7	89.5 \pm 0.6	88.8 \pm 0.5	90.8 \pm 0.6
Gauss. nse	27.7 \pm 5.1	68.8 \pm 0.9	75.4 \pm 0.8	72.3 \pm 0.7	80.6 \pm 0.6
Glass blr	51.3 \pm 1.8	66.7 \pm 0.5	70.6 \pm 1	68.3 \pm 0.6	74.7 \pm 0.9
Impulse nse	25.9 \pm 3.8	62 \pm 1.2	68.8 \pm 0.8	65.5 \pm 0.7	74.5 \pm 0.4
Jpeg compr.	74.9 \pm 1	73.9 \pm 1.2	78.4 \pm 0.9	76.2 \pm 0.9	82.2 \pm 0.5
Motion blr	66.1 \pm 1.7	87 \pm 0.1	88.2 \pm 0.3	87.6 \pm 0.3	89.5 \pm 0.2
Pixelate	48.2 \pm 2.2	80.5 \pm 0.4	83.2 \pm 0.7	81.7 \pm 0.5	86.7 \pm 0.7
Saturate	89.9 \pm 0.4	91.9 \pm 0.1	92.4 \pm 0.1	92.3 \pm 0.2	92.8 \pm 0.2
Shot nse	34.4 \pm 4.9	70.9 \pm 1.2	77.7 \pm 1.6	74.6 \pm 1.3	82.2 \pm 0.6
Snow	76.6 \pm 1.1	82.6 \pm 0.7	84.5 \pm 0.9	83.4 \pm 0.9	86.8 \pm 0.6
Spatter	75 \pm 0.8	83.2 \pm 0.5	86 \pm 0.2	84.6 \pm 0.2	88.6 \pm 0.2
Speckle nse	40.7 \pm 3.7	70.2 \pm 0.7	77.2 \pm 0.6	74.2 \pm 0.6	82.4 \pm 0.2
Zoom blr	60.5 \pm 5.1	88 \pm 0.4	89.4 \pm 0.2	88.6 \pm 0.3	90.7 \pm 0.2
Avg.	57.8 \pm 0.7	80.3 \pm 0	83.2 \pm 0.2	81.8 \pm 0.2	85.9 \pm 0.3

Table 19: CIFAR-10-C *online* ECE (%) results. Shown are the mean and 1 standard deviation.

	Src-only	AdaBN	IM	TENT	FR
Brightness	4.7 \pm 0.2	5.4 \pm 0.2	5.1 \pm 0.3	5.1 \pm 0.2	4.9 \pm 0.3
Contrast	43.5 \pm 2.8	6.8 \pm 0.4	8.7 \pm 0.5	7.6 \pm 0.5	6.1 \pm 0.4
Defocus blr	28.2 \pm 4	7.1 \pm 0.4	6.7 \pm 0.3	7 \pm 0.3	6.4 \pm 0.3
Elastic	12.4 \pm 0.7	13.5 \pm 0.3	12.7 \pm 0.4	12.9 \pm 0.5	12.3 \pm 0.4
Fog	17.4 \pm 2.1	8.4 \pm 0.6	8.3 \pm 0.3	8.3 \pm 0.4	7.3 \pm 0.5
Frost	22.7 \pm 1.7	11.2 \pm 0.7	10.9 \pm 0.5	11 \pm 0.5	9 \pm 0.6
Gauss. blr	40.7 \pm 6.2	7.3 \pm 0.4	6.8 \pm 0.4	7 \pm 0.3	6.3 \pm 0.4
Gauss. nse	57.6 \pm 6.7	19.2 \pm 0.7	16 \pm 0.6	17.6 \pm 0.4	13.2 \pm 0.6
Glass blr	31.2 \pm 1.3	21.4 \pm 0.6	19.6 \pm 0.7	20.7 \pm 0.5	17.9 \pm 0.7
Impulse nse	51.2 \pm 4	23.8 \pm 0.9	20.6 \pm 0.8	22.2 \pm 0.4	17.9 \pm 0.4
Jpeg compr.	14.6 \pm 0.8	16.3 \pm 0.9	14 \pm 0.5	15.1 \pm 0.6	12.2 \pm 0.4
Motion blr	21.1 \pm 1.3	7.8 \pm 0.1	7.6 \pm 0.3	7.7 \pm 0.2	7 \pm 0.2
Pixelate	36.9 \pm 2.5	12 \pm 0.4	10.8 \pm 0.6	11.5 \pm 0.5	8.9 \pm 0.5
Saturate	5.5 \pm 0.3	5.1 \pm 0.1	5 \pm 0.1	5.1 \pm 0.1	4.9 \pm 0.2
Shot nse	50.2 \pm 5.9	17.9 \pm 0.9	14.3 \pm 1.1	16 \pm 0.8	12 \pm 0.5
Snow	14.3 \pm 0.5	10.7 \pm 0.3	9.9 \pm 0.6	10.4 \pm 0.6	8.9 \pm 0.5
Spatter	16.9 \pm 0.8	10.2 \pm 0.4	9.1 \pm 0.2	9.6 \pm 0.2	7.6 \pm 0.2
Speckle nse	43.2 \pm 4.5	18.8 \pm 0.5	14.8 \pm 0.5	16.3 \pm 0.5	11.9 \pm 0.2
Zoom blr	24.4 \pm 3.5	7.3 \pm 0.3	6.8 \pm 0.2	7.1 \pm 0.2	6.3 \pm 0.1
Avg.	28.2 \pm 0.4	12.1 \pm 0	10.9 \pm 0.1	11.5 \pm 0.1	9.5 \pm 0.2

A.8.8 CIFAR-100-C full online results

Tables 20 and 21 show the accuracy and ECE results for each individual corruption of CIFAR-100-C when adapting in an *online* fashion (see Appendix A.8.2). It is worth noting that FR achieves the biggest wins on the most severe shifts, i.e. those on which AdaBN (Li et al., 2017) performs poorly.

Table 20: CIFAR-100-C *online* accuracy (%) results. Shown are the mean and 1 standard deviation.

	Src-only	AdaBN	IM	TENT	FR
Brightness	63.2 \pm 1.1	66.1 \pm 0.4	69.3 \pm 0.9	69.9 \pm 0.7	69.4 \pm 0.4
Contrast	13.9 \pm 0.6	61.4 \pm 0.5	64.8 \pm 0.5	66.6 \pm 1.1	64.5 \pm 0.3
Defocus blr	35.9 \pm 0.7	65.6 \pm 0.1	69 \pm 0.1	69.4 \pm 0.3	68.6 \pm 0.2
Elastic	58.5 \pm 0.7	60.4 \pm 0.2	63.3 \pm 0.5	63.7 \pm 0.1	63.4 \pm 0.3
Fog	36.9 \pm 0.5	55.4 \pm 0.6	61 \pm 0.5	62.5 \pm 0.7	61.7 \pm 0.5
Frost	41.1 \pm 0.9	55.3 \pm 0.6	60.5 \pm 1	61.8 \pm 0.6	60.8 \pm 0.8
Gauss. blr	28.2 \pm 1	64.3 \pm 0.3	68.6 \pm 0.2	69 \pm 0.6	68.4 \pm 0.5
Gauss. nse	11.9 \pm 1.2	43.8 \pm 0.6	53.5 \pm 0.2	55.1 \pm 0.5	54.7 \pm 0.3
Glass blr	45.1 \pm 0.9	53.3 \pm 0.6	57.8 \pm 0.4	58.2 \pm 0.5	57.9 \pm 0.5
Impulse nse	7.2 \pm 0.8	40.8 \pm 0.5	50.2 \pm 0.4	50.9 \pm 0.7	51.7 \pm 0.8
Jpeg compr.	48.6 \pm 0.9	49.8 \pm 0.7	56 \pm 0.2	57.2 \pm 0.2	56.6 \pm 0.6
Motion blr	45.1 \pm 0.5	63.4 \pm 0.2	66.4 \pm 0.4	66.7 \pm 0.6	66 \pm 0.3
Pixelate	22.3 \pm 0.4	59.4 \pm 0.6	65.1 \pm 0.7	67.1 \pm 0.4	65.6 \pm 0.6
Saturate	55.8 \pm 0.4	65.7 \pm 0.4	69.5 \pm 0.6	69.5 \pm 0.6	69.3 \pm 0.4
Shot nse	14.1 \pm 1.2	44.6 \pm 0.9	54.9 \pm 0.1	55.5 \pm 0.4	56.4 \pm 0.3
Snow	49.4 \pm 0.8	53.5 \pm 0.4	59.7 \pm 1.1	61.6 \pm 0.8	60.5 \pm 0.5
Spatter	54.8 \pm 1.1	64.9 \pm 0.6	71.3 \pm 0.5	70.6 \pm 0.6	71.6 \pm 0.7
Speckle nse	15.6 \pm 1.3	42.3 \pm 1	54.2 \pm 0.3	54.9 \pm 0.3	55.8 \pm 0.6
Zoom blr	45.1 \pm 0.7	65.9 \pm 0.3	68.9 \pm 0.6	69 \pm 0.4	68.8 \pm 0.3
Avg.	36.4 \pm 0.5	56.6 \pm 0.3	62.3 \pm 0.3	63.1 \pm 0.3	62.7 \pm 0.3

Table 21: CIFAR-100-C *online* ECE (%) results. Shown are the mean and 1 standard deviation.

	Src-only	AdaBN	IM	TENT	FR
Brightness	6.3 \pm 0.3	11.4 \pm 0.1	11.6 \pm 0.4	11.9 \pm 0.2	10.9 \pm 0.2
Contrast	37.8 \pm 2.2	12.5 \pm 0.2	14.6 \pm 0.3	14.1 \pm 0.6	12.5 \pm 0.2
Defocus blr	16 \pm 0.8	11.4 \pm 0.2	11.3 \pm 0.2	11.8 \pm 0.2	11.4 \pm 0.3
Elastic	8 \pm 0.1	12.7 \pm 0.2	12.9 \pm 0.2	13.4 \pm 0.3	13 \pm 0.2
Fog	21 \pm 0.6	13.8 \pm 0.2	13.9 \pm 0.2	14.4 \pm 0.2	13.6 \pm 0.3
Frost	14.1 \pm 1.1	14.5 \pm 0.2	14.5 \pm 0.6	14.8 \pm 0.3	13.9 \pm 0.4
Gauss. blr	20.5 \pm 1.4	11.9 \pm 0.3	11.6 \pm 0.4	11.9 \pm 0.2	11.9 \pm 0.4
Gauss. nse	39.3 \pm 5.5	17.7 \pm 0.3	16.7 \pm 0.3	17.2 \pm 0.7	16.5 \pm 0.3
Glass blr	15.7 \pm 1.1	15 \pm 0.1	15.2 \pm 0.5	16.1 \pm 0.3	15.1 \pm 0.1
Impulse nse	35.1 \pm 2.6	18.4 \pm 0.2	18.1 \pm 0.2	19.4 \pm 0.5	17.9 \pm 0.3
Jpeg compr.	8.6 \pm 0.2	16.2 \pm 0.3	15.9 \pm 0.1	16.4 \pm 0.4	16.2 \pm 0.2
Motion blr	12.2 \pm 0.2	12.2 \pm 0.2	12.2 \pm 0.3	12.9 \pm 0.2	12.5 \pm 0.2
Pixelate	27.5 \pm 1	13 \pm 0.3	12.5 \pm 0.3	12.4 \pm 0.1	12.3 \pm 0.2
Saturate	8.8 \pm 0.2	11.4 \pm 0.1	11.3 \pm 0.3	11.7 \pm 0.4	11.3 \pm 0.4
Shot nse	37.2 \pm 5.9	17.2 \pm 0.3	16.4 \pm 0.2	17.5 \pm 0.7	16.2 \pm 0.3
Snow	8.5 \pm 0.3	15.6 \pm 0.2	15 \pm 0.4	14.7 \pm 0.3	14.8 \pm 0.1
Spatter	6.7 \pm 0.3	11.4 \pm 0.2	10.7 \pm 0.2	11.3 \pm 0.3	10.7 \pm 0.3
Speckle nse	34.5 \pm 5.4	18.2 \pm 0.4	16.5 \pm 0.4	17.5 \pm 0.3	16.1 \pm 0.4
Zoom blr	10.5 \pm 0.3	11.2 \pm 0.2	11.2 \pm 0.3	11.6 \pm 0.3	11.4 \pm 0.1
Avg.	19.4 \pm 0.9	14 \pm 0.1	13.8 \pm 0.1	14.3 \pm 0.1	13.6 \pm 0.1

A.9 Further implementation details

Architectures. For digit and character datasets we use a simple 5-layer CNN which is a variant of LeNet (LeCun et al., 1998)—details are provided in Table 22. For the object-recognition datasets, we use ResNet-18 (He et al., 2016).

Tracking feature and logit distributions. To track the marginal feature and logit distributions, we implement a simple `StatsLayer` class in PyTorch that can be easily inserted into a network just like any other layer. This seamlessly integrates distribution-tracking into standard training processes. In the source domain, we simply: (i) add `StatsLayers` to our (pre)trained source model; (ii) pass the source data through the model; and (iii) save the model as normal in PyTorch (the tracked statistics, i.e. bin counts, are automatically saved as persistent buffers akin to BN-statistics). In the target domain, the source model can be loaded as normal and the inserted `StatsLayer`s will contain the source-data statistics. Code is available at <https://github.com/cianeastwood/bufr>.

Online setup. In the online setting, where only a single epoch is permitted, we find that all methods are very sensitive to the learning rate (unsurprising, given that most methods will not have converged after a single epoch). For fair comparison, we thus search over learning rates in $\{0.1, 0.01, 0.001, 0.0001\}$ for all methods, choosing the best-performing one. Additionally, when learning speed is of critical importance, we find it beneficial to slightly increase τ . We thus set $\tau = 0.05$ for all online experiments, compared to 0.01 for all “offline” experiments.

Table 22: Architecture of the CNN used on digit and character datasets. For conv. layers, the weights-shape is: *num. input channels* \times *num. output channels* \times *filter height* \times *filter width*.

Block	Weights-Shape	Stride	Padding	Activation	Dropout Prob.
Conv + BN	$3 \times 64 \times 5 \times 5$	2	2	ReLU	0.1
Conv + BN	$64 \times 128 \times 3 \times 3$	2	2	ReLU	0.3
Conv + BN	$128 \times 256 \times 3 \times 3$	2	2	ReLU	0.5
Linear + BN	6400×128	N/A	N/A	ReLU	0.5
Linear	$128 \times \text{Number of Classes}$	N/A	N/A	Softmax	0

A.10 Further analysis

Figure 17a shows that, on average, FR moves the weights of all layers of g_t a similar distance when adapting to the target data. Figure 17b shows that BUFR primarily updates the early layers, thus preserving learnt structure in later layers.

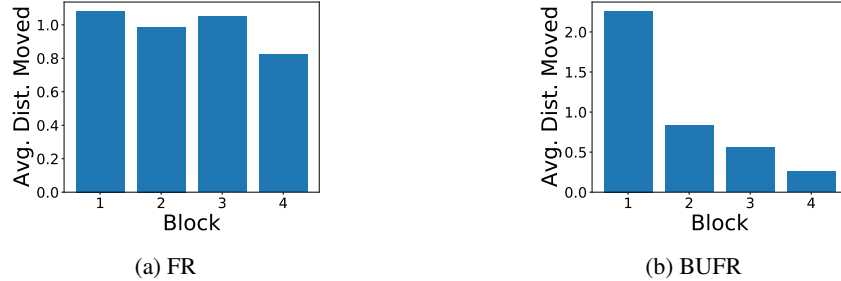


Figure 17: Average distance moved by a unit in each block of g_t on the EMNIST-DA stripe shift when training (a) all layers at once and (b) in a bottom-up manner. Both methods are trained with the same constant learning rate.

A.11 Notations

Table 23 summarizes the notations used in the paper.

Table 23: Notations.

	Symbol	Description
Distributions	$p_{\mathbf{z}}$	Source feature distribution
	$q_{\mathbf{z}}$	Target feature distribution
	p_{z_d}	Source d -th marginal feature distribution
	q_{z_d}	Target d -th marginal feature distribution
	$\pi_{\mathbf{z}}^s$	Source approx. marginal feature distributions
	$\pi_{\mathbf{z}}^t$	Target approx. marginal feature distributions
	$\pi_{z_d}^s$	Source d -th approx. marginal feature distribution
	$\pi_{z_d}^t$	Target d -th approx. marginal feature distribution
	$\pi_{\mathbf{a}}^s$	Source approx. marginal logit distributions
	$\pi_{\mathbf{a}}^t$	Target approx. marginal logit distributions
	$\pi_{a_k}^s$	Source k -th approx. marginal logit distribution
	$\pi_{a_k}^t$	Target k -th approx. marginal logit distribution
Sets	\mathcal{D}_s	Labelled source dataset
	\mathcal{D}_t	Unlabelled target dataset
	\mathcal{X}_s	Input-set of the source domain
	\mathcal{X}_t	Input-set of the target domain
	\mathcal{Y}_s	Label-set of the target domain
	\mathcal{Y}_t	Label-set of the target domain
Network	f_s	Source model, $f_s = h(g_s(\cdot))$
	f_t	Target model, $f_t = h(g_t(\cdot))$
	g_s	Source feature-extractor
	g_t	Target feature-extractor
	h	Classifier (or regressor)
Other	\mathbf{u}	Soft-binning function
	z_d^{min}	Minimum value of feature d (on the source data)
	z_d^{max}	Maximum value of feature d (on the source data)
	τ	Temperature parameter for soft binning